

REPORT DOCUMENTATION PAGE

AFRL-SR-BL-TR-99-

Public reporting burden for this collection of information is estimated to average 1 hour per response gathering and maintaining the data needed, and completing and reviewing the collection of information, including suggestions for reducing this burden, to Washington Headquarters, Davis Highway, Suite 1204, Arlington, VA 22202-4302, and to the Office of Management and Budget

data sources,
spect of this
15 Jefferson
503.

1. AGENCY USE ONLY (Leave blank)

2. REPORT DATE

3.

1/29/99

Final Technical Report 8-1-96 to 6-30-98

4. TITLE AND SUBTITLE

Experimental and Numerical Investigations on Failure Mechanisms in
Fiber-Reinforced Ceramics

5. FUNDING NUMBERS

F49620-95-1-0262

6. AUTHOR(S)

H. L. Schreyer
M. L. Wang

61102F
2302/BS

7. PERFORMING ORGANIZATION NAME(S) AND ADDRESS(ES)

H. L. Schreyer, University of New Mexico, Department of Mechanical Engineering
Albuquerque, NM 87131

M. L. Wang, University of Illinois at Chicago, Department of Civil & Materials
Engineering, 842 West Taylor, Chicago, IL 60607-7023

8. PERFORMING ORGANIZATION
REPORT NUMBER

9. SPONSORING/MONITORING AGENCY NAME(S) AND ADDRESS(ES)

Air Force Office of Scientific Research/NA
801 N. Randolph Street, Rm 732
Arlington, VA 22203-1977

10. SPONSORING/MONITORING
AGENCY REPORT NUMBER

F49620-95-1-0262

11. SUPPLEMENTARY NOTES

12a. DISTRIBUTION AVAILABILITY STATEMENT

Approved for public release; distribution unlimited.

12b. DISTRIBUTION CODE

A

13. ABSTRACT (Maximum 200 words)

The primary focus on this research was to model the evolution of microcracks at the interfaces of grains and inclusions in quasibrittle materials. Several unique aspects have been developed as part of the research. These include the application of the material point method to a new class of problems and the formulation of a thermodynamically-based decohesion constitutive equation. In addition, numerical algorithms were formulated to handle three-dimensional problems, to include the effects of randomness of grain sizes and of the strength of cement paste, and to take into account boundary constraints. Each of these aspects represent new or extensive improvements to the approaches available at the time the research was initiated.

14. SUBJECT TERMS

15. NUMBER OF PAGES

48

16. PRICE CODE

17. SECURITY CLASSIFICATION
OF REPORT

Unclassified

18. SECURITY CLASSIFICATION
OF THIS PAGE

Unclassified

19. SECURITY CLASSIFICATION
OF ABSTRACT

Unclassified

20. LIMITATION OF
ABSTRACT

UL

0 9 FEB 1999

Original

Final Report for the Period: 1 Aug. 1996 - 30 June 1998

**EXPERIMENTAL AND NUMERICAL INVESTIGATIONS ON FAILURE
MECHANISMS IN FIBER-REINFORCED CERAMICS**

by

H.L. Schreyer

Department of Mechanical Engineering
University of New Mexico
Albuquerque, NM 87111

and

M.L. Wang

Department of Civil and Materials Engineering
University of Illinois at Chicago
842 West Taylor Street
Chicago, IL 60607-7023

AFOSR Grant F49620-95-1-0262
(Started 1 April 1995)

Submitted to:

Dr. Ozden O. Ochoa

Mechanics and Materials Program
AFOSR/NA
110 Duncan Ave., B115
Bolling AFB, DC 20332-8080

January 1999

19990302049

Approved for public release;
distribution unlimited.

EXECUTIVE SUMMARY

The addition of spherical inclusions and fibers into a traditional ceramic matrix can provide enhanced ductility and toughness over that of the monolithic ceramic. The primary objective of the research was to provide an improved microstructural understanding of a fiber-reinforced composite material. To properly identify the fundamental issues, a combination of expertise in experimental methodology and of the formulation of advanced constitutive equations is required. Experimental data shows the dominant failure mechanisms and the theoretical investigation focuses on these features.

Preliminary experimental data for a particular alumina showed that failure occurred almost exclusively along grain boundaries. The obvious conclusion is that the properties of material that constitute grain boundaries must have a dominating influence on the failure mode and strength of the ceramic. A second observation was that there did not appear to be a microcrack-cloud zone, a result that is contrary to some reports in the literature. Instead, microcrack branches form along grain boundaries with one microcrack eventually becoming dominant to the point where all contact is lost at which time the adjacent microcracks become inactive. The process can be thought of as decohesion in which traction carrying capability is gradually reduced to zero as a microcrack evolves to a macrocrack. This procedure is also called material failure.

Microcracks actually represent a strong discontinuity in displacement, a feature that is particularly difficult to represent both theoretically and numerically. Since failure along the boundaries of inclusions and fibers is also one of an evolving microcrack, the key component to being able to analyze a whole class of problems is that of modeling decohesion. Simultaneously, there is the problem of obtaining a robust numerical solution procedure.

A team at the University of New Mexico has been in the forefront of the development of a numerical scheme applicable to a wide range of problems in continuum mechanics called the Material Point Method (MPM). Part of this research involved investigating the suitability of the method for handling material failure. Simultaneously, a thermodynamically-based derivation of a decohesion model was developed to the point where the evolution of decohesion could be handled through a constitutive equation. This precludes the need for special elements, realignment of elements or of continuous remeshing as a crack propagates. Because a length scale is a natural part of a decohesive constitutive equation, convergence with mesh refinement can be expected and is, indeed, shown. Schreyer, Sulsky and Zhou have provided a study of ceramic grains showing the potential effect of how damage may evolve with cooling.

A true representation of the behavior of quasibrittle materials must take into account both the three-dimensional nature of the problem and the randomness of grain sizes and the strength of cement paste. Wang and Chen have provided both numerical and experimental data to show that such a fundamental approach can provide the observed features of failure including the important effects of boundary constraints.

It was quickly realized that a comprehensive study of the effects of inclusions and fibers could only be performed provided a complete description of the matrix material is understood. Therefore, the direction of the research became more fundamental and concentrated on grains and inclusions, and their boundaries. Results of these efforts are provided by three papers reproduced here as sections of the final report.

TABLE OF CONTENTS

	PAGE
1. EXECUTIVE SUMMARY	ii
2. Paper: H.L. Schreyer, D.L. Sulsky and S.-J. Zhou, "Modeling Material Failure as a Strong Discontinuity with the Material Point Method," To appear in the Proceedings of a Workshop on Mechanics of Quasi-Brittle Materials and Structures in honor of the 60'th birthday of Prof. Z.P. Bazant , 27-28 March, 1998 Prague, The Czech Republic.	2
3. Paper: M.L. Wang and Z.L. Chen, "Experimental and Numerical Investigations of Concrete Failure under Triaxial Loading," Proceedings FRAMCOS-3, Fracture Mechanics of Concrete Structures, AEDIFICATIO Publishers, D-79014 , 1998, Freiburg, Germany.	23
4. Paper: M.L. Wang and Z.L. Chen, "Simulation of the Failure Mechanisms of Quasi-Brittle Materials," Proceedings of Kumamoto International Workshop on Fracture Mechanics and Acoustic Emission in Concrete , Oct. 18-19, 1998, Kumamoto, Japan.	33

MODELING MATERIAL FAILURE AS A STRONG DISCONTINUITY WITH THE MATERIAL POINT METHOD

Howard L. Schreyer¹, Deborah L. Sulsky²
and S.-J. Zhou¹

¹*Dept, of Mechanical Engineering*

²*Dept, of Mathematics and Statistics*

University of New Mexico

Albuquerque, NM USA 87131

ABSTRACT:

A discrete constitutive equation for modeling material failure as a decohesion or separation of material to form two free surfaces is a relatively simple approach. However, numerical simulations based on such a model involve considerable complexity including remeshing if the finite element approach is used. Here, a basic formulation involving the simultaneous application of the continuum and decohesion constitutive equations is described together with a numerical approach based on the material point method. Preliminary results indicate that failure propagation can be predicted at an arbitrary angle without the dispersion of the crack front that is often observed with conventional finite elements.

KEY WORDS: *Decohesion, localized deformation, softening, material point method, strong discontinuity.*

1. Introduction

The propagation of cracks through concrete is just a manifestation of material failure. Numerous models of failure have been proposed together with numerical procedures for obtaining solutions to the governing boundary value problem. Unfortunately, the material model for failure is often entwined with the numerical approach so that it is difficult to determine which aspect is the limiting component if predictions do not match experimental data. Here, we attempt to carefully differentiate these two essential components by first concentrating on a basic failure model, and then proposing the use of a relatively new numerical procedure, the material point method. Preliminary results indicate that the difficulties associated with the finite element method are not present.

There are many criteria for material failure but the definitions of failure are often vague or defined implicitly through each criterion. We take material failure to mean the process by which two new free surfaces are formed, with brittle fracture as an obvious example. However, there are other forms of material failure as exemplified by ductile rupture, delamination, the breaking of grain boundaries and the pullout of reinforcing rods or fibers. Our interest is to represent all of these phenomena with a single model that incorporates the essential features of the state of stress or strain at which failure initiates and predicts the correct energy dissipated. Our focus is not on replicating the details of failure, although this can be done in some cases, but on predicting the effect of failure on the far-field stress distribution and on structural response as reflected, for example, by a force-deflection curve. The proposed approach is a constitutive equation that describes decohesion. When used with the material point method, which is a relatively new computational method that is particularly robust for problems with large deformations, the proposed approach has a simple structure in that the decohesion comes into the analysis through the constitutive equation only. There is no attempt to enforce the geometrical continuity of a crack. Instead, compatibility is enforced in an averaged sense.

Failure modeling involves both theoretical formulations of constitutive equations and numerical simulations, and the two aspects should be carefully delineated. However, the finite element method has become the method of choice for the majority of engineering applications so that the formulation of the constitutive equations is often tailored for use by finite elements; conversely limitations imposed by the finite element method are often interpreted unjustly as a limitation of the theoretical approach. In the following brief survey, we attempt to keep the discussion of the two phases distinct if at all possible.

A large number of papers related to failure have been based on a zone of softening with an assumed width in which a continuum constitutive equation continues to be used [BAZ 84, BOR 87, ROT 87, OLI 89, DAH 90, WIE 98]. A theoretical difficulty with such an approach is the possible loss of ellipticity and material stability within the band. When used with finite elements, the band width is associated with the size of the elements and the accuracy is then limited when the elements become highly deformed.

An alternative (discrete) approach is to consider material failure as a strong discontinuity in displacement with traction related to the discontinuity. There is a long history in which discrete constitutive equations are postulated directly as reflected by Barenblatt [BAR 59], and Hillerborg et al. [HIL 76]. Feenstra et al. [FEE 1991] and Corigliano [COR1993] provide a nice summary of previous models and describe numerical methods based on the use of interface elements. The use of discrete constitutive equations has not met with complete favor partially because strong discontinuities are difficult to handle numerically and convergence with mesh refinement and mesh insensitivity is difficult to show. The use of interface elements may require frequent remeshing if the crack surface propagates in a curved manner, and double nodes which separate with the evolution of decohesion [SCH, 1992]. However, Dvorkin et al. [DVO 90] provide a nice approach that overcomes many of these objections by handling discontinuities at the element level rather than enforcing discontinuities to be along element boundaries.

A fundamentally different approach is described in more recent work by Simo et al. [SIM 93] in which the continuum constitutive equation is extended beyond the loss of ellipticity condition into the softening regime. They argue that this extension should be accompanied by distribution theory which, in effect, leads to a strong discontinuity. The theory has since been extensively developed by Oliver [OLI 89], Simo and Oliver [SIM 94], Armero and Garikipati [ARM 95], Larsson and Runesson [LAR 96], Oliver [OLI 96] and Armero [ARM 97]. The final result is discrete constitutive equations relating stress to the discontinuity in displacement, and here also the discontinuity is handled at the element or constitutive level.

We have opted for a particular combination of these ideas in an attempt to provide an approach that is as simple and as straightforward as possible. First, we propose the direct introduction of discrete constitutive equations with the thought that they should be introduced when ellipticity is lost, although a direct failure initiation criterion can be used. No attempt is made to model the post-crack frictional effects that may occur with surfaces with rough cracks [FEE 91] although such features can be added. Second, the discontinuity is considered to be part of the constitutive equation and is applied in a manner analogous to that of Dvorkin [DVO 91], Oliver [OLI 96a, OLI 96b] and Armero [ARM 97]. A point that is undergoing failure is also considered to be a material point in the continuum so that the decohesion and continuum constitutive equations must be simultaneously satisfied subject to the restriction of traction equilibrium. Third, we invoke the constitutive equation in the material point method. The arguments for the direct calculation of the strong discontinuity in displacement, which we also call decohesion, and the use of the material point method are summarized as follows:

- (i) We retain the conceptual simplicity inherent with the discrete constitutive approach that material failure does not happen abruptly but occurs smoothly with a gradual reduction in traction as the displacement discontinuity increases.
- (ii) We believe it is extremely difficult to evaluate properties of any constitutive equation in the failure regime. However, it is probably easier to select material

parameters for a discrete constitutive equation than for a continuum model extended into the softening regime.

(iii) The discrete equation can be applied, if desired, at the instance ellipticity is lost so that there is a high probability that well posedness can be retained although a stability analysis must be performed [SUO 92].

(iv) The essential aspects of prescribed stress at the initiation of failure and prescribed energy dissipation at the end of failure are automatically included in this model.

(v) Once decohesion is initiated on a surface of discontinuity, the adjacent continuum tends to unload into the elastic regime, so the computational simplicity of only needing to combine decohesion with elasticity covers the vast majority of practical cases.

(vi) The decohesion constitutive equation can be developed in a thermodynamical setting, in concert with many current continuum models, and can include plasticity, damage, viscoelastic and viscoplastic features that are associated strictly with the decohesion.

(vii) The application of decohesion constitutive equations in the material point method retains the simplicity of current applications of strong discontinuities at the element level in the finite element method. However, double nodes or interface elements are not needed and there is the additional potential advantage that mesh orientation and mesh distortion are not factors that need to be considered.

(viii) Following the method outlined by Allix and Corigliano [ALL 95, ALL 96] there is the potential of relating the decohesion constitutive equation to mixed-mode fracture.

(ix) Finally, the use of a discrete constitutive equation may still be a suitable model for diffuse failure if the primary objective is to obtain an efficient solution for the region away from the failure zone.

The next section provides only a brief description of the material point method since the method has been fully described in previous papers. Section 3 describes the basic structure of the decohesion model used in our analysis. Analytical and numerical solutions to model problems [ZHO 98] including a convergence study are given in Section 4 which is then followed by conclusions concerning the general applicability of the method for material failure in general including delamination.

2. The Material Point Method

The material point method [SUL 94, SUL 95, SUL 96] discretizes a solid body by marking a set of material points in the original configuration that are tracked throughout the deformation process. Let \mathbf{x}_p^n , $p = 1, \dots, N_p$ denote the current position of material point p at time t^n , $n = 0, 1, 2, \dots$. These material points provide a Lagrangian description of the solid body that is not subject to mesh tangling. Each point at time t^n has an associated mass, m_p , density, ρ_p^n , velocity, \mathbf{v}_p^n , Cauchy stress tensor, $\boldsymbol{\sigma}_p^n$, strain, \mathbf{e}_p^n , and any other internal variables necessary for the constitutive

model. If temperature changes are important, internal energy or temperature may also be ascribed to the material points. The material point mass is constant in time, insuring that the continuity equation is satisfied. Other variables must be updated with reference to conservation of momentum, conservation of energy, or from the constitutive model.

To make the computations tractable, at each timestep of a dynamic algorithm, information from the material points is interpolated to a background computational mesh. This mesh covers the computational domain and is chosen for computational convenience. A particularly simple choice is a regular rectangular grid. After information is interpolated to the grid, equations of motion are solved on this mesh which is considered to be an updated Lagrangian frame. For example, to solve the momentum equation on the grid using an explicit FE algorithm, one must know the value of the momentum at the beginning of the timestep at the nodal positions. The nodal momentum, $m_i^a v_i^a$, is the product of the nodal mass and nodal velocity, and each is determined by interpolation,

$$\begin{aligned} m_i^a &= \sum_{p=1}^{N_p} m_p N_i(\mathbf{x}_p^a) \\ m_i^a v_i^a &= \sum_{p=1}^{N_p} m_p v_p^a N_i(\mathbf{x}_p^a) \end{aligned} \quad (1)$$

In the above, $N_i(\mathbf{x})$ is the nodal basis function associated with node i . In this paper, $N_i(\mathbf{x})$ are the tensor products of piecewise linear functions. The internal forces are determined from the particle stresses according to

$$\mathbf{f}_i^{\text{int}} = - \sum_{p=1}^{N_p} \mathbf{G}_{ip}^a \boldsymbol{\sigma}_p^a m_p / \rho_p^a \quad (2)$$

The quantity \mathbf{G}_{ip}^a is the gradient of the nodal basis function evaluated at the material point position, $\mathbf{G}_{ip}^a = \nabla N_i(\mathbf{x})|_{\mathbf{x}_p^a}$. The momentum equation is solved with the nodes considered to be moving with the deformation to give nodal velocities, v_i^t , at the end of this Lagrangian timestep of size Δt ,

$$m_i^a \frac{v_i^t - v_i^a}{\Delta t} = \mathbf{f}_i^{\text{int}}. \quad (3)$$

At the end of this Lagrangian step, the new nodal values of velocity are used to update the material points. The material points move along with the nodes according to the solution given throughout the elements by the nodal basis functions

$$\mathbf{x}_p^{a+1} = \mathbf{x}_p^a + \Delta t \sum_{i=1}^{N_n} v_i^t N_i(\mathbf{x}_p^a). \quad (4)$$

Similarly, the material point velocity is updated via

$$\mathbf{v}_p^{a+1} = \mathbf{v}_p^a + \sum_{i=1}^{N_n} (v_i^t - v_i^a) N_i(\mathbf{x}_p^a). \quad (5)$$

The sums in these last two equations extend from 1 to N_n where N_n is the number of nodes in the computational mesh.

A strain increment for each material point is determined using the gradient of the nodal basis function,

$$\Delta \mathbf{e}_p^a = \frac{\Delta t}{2} \sum_{i=1}^{N_n} [\mathbf{G}_{ip}^a v_i^t + (\mathbf{G}_{ip}^a v_i^t)^T]. \quad (6)$$

This strain increment is then used in an appropriate constitutive equation for the material being modeled to update the stress at the material point. Any internal variables necessary in the constitutive model can also be assigned to the material points and transported along with them. Once the material points have been completely updated, the computational mesh may be discarded and a new mesh defined, if desired, and then the next timestep is begun.

The material point method has several advantages. The Lagrangian description provided by the material points can undergo large deformations without mesh tangling. Since the computational mesh is under user control, it can be chosen so that reasonable timesteps may be taken in this Lagrangian frame. Usually, the timestep is restricted by the CFL condition for an explicit algorithm, where the critical timestep is the ratio of the mesh size to the wave speed. Note that this condition depends on the more favorable mesh spacing, not the material point spacing. Since equations are solved in an updated Lagrangian frame on the FE mesh, the nonlinear convective terms troublesome in Eulerian formulations, are not an issue. Finally, the material points transport material properties and internal variables without error.

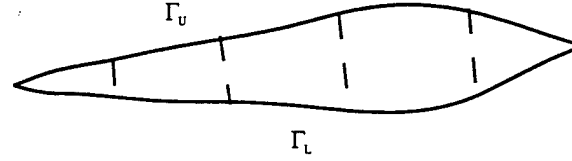
3. Discrete Constitutive Equation For Decohesion

3.1 The Theoretical Model

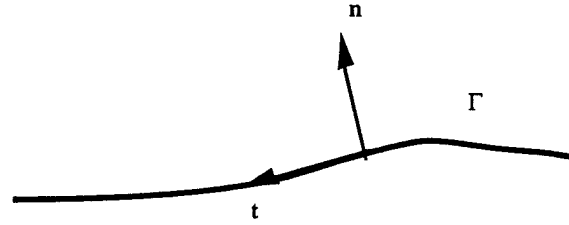
We define the initiation of material failure as the time when a material point first experiences a discontinuity in displacement but continues to function as a point in a solid continuum. A collection of such points in a neighborhood defines a failure surface, Γ . Although the material manifestation is a single surface, one observes spatially two surfaces, Γ_U and Γ_L , as sketched in Fig. 1. Each dotted line illustrates points in space identified with a single material point which can be considered associated with any one of the spatial points on the line. The sketch illustrates the material surface as a thick line between the two spatial surfaces but if a Lagrangian description is used, the material surface may be at a totally different location. Failure is said to be complete when traction can no longer be sustained on the material surface, i.e., the spatial surfaces no longer have any ligaments connecting them even though one point on each surface is identified as a single material point. The discontinuity in displacement is called decohesion.

Here, we present a development of discrete constitutive equations using thermodynamics as a framework with the result that the dissipation inequality is automatically satisfied. The approach entails two essential assumptions consisting of (1) the form of the free energy, and (2) the form of the evolution equations. Each assumption leads to a different model which can only be tested by solving a problem for which either qualitative or quantitative data exist. To allow for the presentation

of different models in a convenient manner, we present the general framework first, and then show the implications inherent in specific assumptions.



(a) Decohesion in spatial configuration - two surfaces.



(b) Decohesion in material configuration - surface with discontinuities

Fig. 1. Material failure as represented by two spatial surfaces, Γ_U and Γ_L , or one material surface, Γ .

The approach is analogous to what one might use for a rigid-plastic continuum for which the elastic part of the response is ignored, i.e., the total strain and the plastic strain are identical. The internal strain energy does not exist and the stress must be provided by the solution to a boundary value problem. However, there remains a contribution to the free energy associated with hardening and evolution equations for plasticity variables.

Consider a situation where loads are applied to a body which is continuous except on a material failure surface, Γ , which displays a strong discontinuity, or decohesion, $\mathbf{u}^d = [\mathbf{u}]$. Any point on the surface is also a point in the continuum which is assumed to be governed by linear elasticity so that the stress, $\boldsymbol{\sigma}$, and strain, \mathbf{e} , are linearly related by the elasticity tensor, \mathbf{E} :

$$\boldsymbol{\sigma} = \mathbf{E}:\mathbf{e} \quad (7)$$

If \mathbf{n} denotes the normal to the surface, then the traction, $\boldsymbol{\tau}$, is given by $\boldsymbol{\tau} = \boldsymbol{\sigma} \cdot \mathbf{n}$. The rate at which power is being added to the surface by this traction is $\boldsymbol{\tau} \cdot \dot{\mathbf{u}}^d$ in which a superposed dot denotes a derivative with respect to time. We postulate that the free energy per unit surface area consists of an initial energy, U_0 , due to residual stresses that resulted from the curing process, and a term, U_d , which represents the effect of decohesion:

$$U = U_0 - U_d(\bar{u}) \quad (8)$$

The use of the negative sign is meant to suggest that normally energy is provided by the original material to the decohesion process. The parameter, \bar{u} , is a scalar representation of the state of decohesion. The specific choice for U_d (positive) is part of a particular model. The decohesion, \mathbf{u}^p , is viewed as "permanent" decohesion and is introduced similarly to plastic strain in elasto-plastic continuum models. In the absence of elasticity, $\mathbf{u}^p = \mathbf{u}^d$.

If only \mathbf{u}^p and \bar{u} are considered to be the primary variables describing decohesion, the dissipation rate is

$$D_s = \boldsymbol{\tau} \cdot \dot{\mathbf{u}}^d - \dot{U} = \boldsymbol{\tau} \cdot \dot{\mathbf{u}}^p + \bar{\tau} \dot{\bar{u}} \quad \text{with} \quad \bar{\tau} = \frac{\partial U_d}{\partial \bar{u}} \quad (9)$$

The generalized traction, $\bar{\tau}$, is conjugate to \bar{u} . Instead of the traction starting at zero, as it does for some existing discrete models [NEE 87, COR 93], we visualize that when the failure process starts, $\mathbf{u}^d = 0$, $\mathbf{u}^p = 0$, and the traction is the initial vector, $\boldsymbol{\tau}_0$ which depends on the path.

We parameterize the development of decohesion through a single, dimensionless monotonically increasing variable, λ , and the evolution equations

$$\dot{\mathbf{u}}^p = \lambda \mathbf{m}^e \quad \dot{\bar{u}} = \lambda m^e \quad (10)$$

in which \mathbf{m}^e and m^e denote evolution functions that depend on $\boldsymbol{\tau}$ and $\bar{\tau}$. \mathbf{m}^e is a vector whose inner product with $\boldsymbol{\tau}$ is assumed to be positive, semi-definite. If we introduce an effective traction

$$\boldsymbol{\tau}^e = \boldsymbol{\tau} \cdot \mathbf{m}^e \quad (11)$$

then the dissipation rate becomes

$$D_s = \lambda [\boldsymbol{\tau}^e + \bar{\tau} m^e] \quad (12)$$

To ensure the dissipation is positive, define a decohesion function as follows:

$$F_d = \boldsymbol{\tau}^e + \bar{\tau} m^e - F_0 \quad F_0 > 0 \quad (13)$$

The function has been constructed in the usual manner so that F_d is negative when the tractions are zero. We assume decohesion does not occur unless $F_d = 0$ in which case the dissipation rate becomes $D_s = \lambda F_0$, a positive scalar (and $F_d > 0$ is not permitted). The evolution equations can now be interpreted as parameterized in terms of dissipation which is a monotonically increasing parameter. The total dissipated energy is simply $D = \lambda F_0$ which depends only on the value of λ and not on the path followed to achieve a given value of λ .

Next, we consider the decohesion condition, $F_d = 0$. At the initiation of decohesion, $\boldsymbol{\tau} = \boldsymbol{\tau}_0$ and $\mathbf{m}^e = \mathbf{m}_0^e$. If we assume $\bar{\tau} = 0$ at the initiation, then

$$F_0 = \boldsymbol{\tau}_0^e \equiv \boldsymbol{\tau}_0 \cdot \mathbf{m}_0^e \quad (14)$$

and the decohesion condition reduces to

$$\boldsymbol{\tau}^e = \boldsymbol{\tau}_0^e - \bar{\tau} m^e \quad (15)$$

Typically, $\bar{\tau}$ increases to the point where $\boldsymbol{\tau}^e$ goes to zero and $\bar{\tau} = \bar{\tau}_s \equiv \boldsymbol{\tau}_0^e / m_s^e$ which is defined to be separation. The values of \mathbf{u}^p and \bar{u} at separation are denoted by \mathbf{u}_s^p and \bar{u}_s , respectively. Unless there is a load reversal which brings the two spatial surfaces back into contact, it is assumed that $\boldsymbol{\tau}^e$ remains zero after separation.

With the use of (8), the stored surface energy lost due to separation is

$$\Phi_U = -U_d(\bar{u}_d) \quad (16)$$

The total energy per unit area that must be provided to cause total separation is variously called the fracture energy, or the energy of separation, Φ_F , and consists of the sum of the stored energy and the dissipated energy:

$$\Phi_F = \Phi_U + \Phi_D \quad (17)$$

Because Φ_U is negative, the fracture energy is less than the dissipation.

In summary, the resulting set of constitutive equations in rate form becomes

$$\begin{aligned} \text{(i)} \quad \dot{\boldsymbol{\sigma}} &= \mathbf{E} : \dot{\boldsymbol{\epsilon}} && \text{Continuum elasticity} \\ \text{(ii)} \quad \dot{\mathbf{t}} &= \dot{\boldsymbol{\sigma}} \cdot \mathbf{n} && \text{Traction equilibrium} \\ \text{(iii)} \quad \dot{\mathbf{m}}^e &= \dot{\lambda} \mathbf{m}^e \quad \dot{\bar{u}} = \dot{\lambda} m^e && \text{Evolution equations} \\ \text{(iv)} \quad \bar{\tau} &= \frac{\partial U_d}{\partial \bar{u}} && \text{Constitutive equation} \\ \text{(v)} \quad F_d &\equiv \tau^e - (\tau_0^e - \bar{\tau} m^e) = 0 && \text{Consistency} \\ \text{(vi)} \quad \tau^e &= \boldsymbol{\tau} \cdot \mathbf{m}^e \quad \text{and} \quad \tau_0^e = \boldsymbol{\tau}_0 \cdot \mathbf{m}_0^e \end{aligned} \quad (18)$$

Two additional assumptions remain to completely formulate constitutive equations; (i) the form of the evolution equations for the evolution functions m^e and \bar{u} , and (ii) the form of the function U_d which provides a constitutive relation between $\bar{\tau}$ and \bar{u} . Even slight changes in the forms of these assumptions can have significant effects on predictions. Since the only possible way to evaluate the suitability of decohesive constitutive equations is indirectly through comparisons of solutions to problems with features provided by experimental data, we consider (18) to be the basic format and provide different models based on plausible assumptions. The results of choosing specific forms for \mathbf{m}^e , m^e and U_d are given next.

3.2 Model 1: Associated Evolution Equations

Here we are more specific in our formulation of the decohesion model. In the theoretical formulation, it is most convenient to use dimensional parameters so that physical interpretations can be easily made; conversely, for numerical implementation of the theory, dimensionless variables should be used. With these objectives in mind, we choose λ to be dimensionless and consider \bar{u} to have the dimension of length (in analogy with the decohesion \mathbf{u}^d). We choose the evolution functions and the decohesion energy to be of the following forms:

$$\mathbf{m}^e = \bar{u}_0 \frac{\mathbf{A}_d \cdot \boldsymbol{\tau}}{(\boldsymbol{\tau} \cdot \mathbf{A}_d \cdot \boldsymbol{\tau})^{1/2}} \quad m^e = \bar{u}_0 \quad U_d = U_0 \frac{(\bar{u} / \bar{u}_0)^{q+1}}{(q+1)} \quad (19)$$

in which \mathbf{A}_d is taken to be a positive definite (dimensionless) tensor whose components are material parameters, as is $q \geq 0$. Additional material parameters (constants) are the reference decohesion scalar, \bar{u}_0 , and the reference surface energy, U_0 . We define a reference scalar traction, $\bar{\tau}_0$, by the relation $U_0 = \bar{u}_0 \bar{\tau}_0$. The immediate result of these choices is that

$$\tau^e = \bar{u}_0 (\boldsymbol{\tau} \cdot \mathbf{A}_d \cdot \boldsymbol{\tau})^{1/2} \quad \bar{u} = \lambda \bar{u}_0 \quad \bar{\tau} = \bar{\tau}_0 (\lambda)^q \quad (20)$$

and the evolution functions are obtained as derivatives of the damage function with respect to the corresponding conjugate variables, i.e., the evolution functions are said to be "associated":

$$\mathbf{m}^* = \frac{\partial F_d}{\partial \tau} \quad \mathbf{m}^* = \frac{\partial F_d}{\partial \bar{\tau}} \quad (21)$$

At this point we consider a two-dimensional formulation with \mathbf{n} denoting the normal to the failure surface and \mathbf{t} a unit tangent vector as indicated in Fig. 1. Corresponding components of τ are τ_n and τ_t , respectively. If the traction consists only of a normal component, specify the failure initiation value as τ_{nf} and, similarly, let τ_{tf} denote the failure initiation value for a purely shear case. One approach for incorporating these failure initiation conditions is to choose the components of A_d with respect to this local basis as follows:

$$[A_d] = \bar{\tau}_0^2 \begin{bmatrix} \frac{1}{(\tau_{nf})^2} & 0 \\ 0 & \frac{1}{(\tau_{tf})^2} \end{bmatrix} \quad (22)$$

The consequences of this choice are

$$\begin{aligned} D_s &= \lambda U_0 & \bar{\tau}^* &= \lambda^q & F_d &= U_0 F_d^* & F_d^* &= \tau^{**} - (1 - \bar{\tau}^*) \\ \tau^* &= U_0 \tau^{**} & \tau^{**} &= \frac{(\tau \cdot A_d \cdot \tau)^{1/2}}{\bar{\tau}_0} = \left(\frac{\tau_n^2}{\tau_{nf}^2} + \frac{\tau_t^2}{\tau_{tf}^2} \right) \end{aligned} \quad (23)$$

where τ^{**} is a dimensionless effective traction, $\bar{\tau}^*$ is a dimensionless form of $\bar{\tau}$, and F_d^* is a dimensionless decohesion function. In deriving these equations, the identities $F_0 = \tau_0^2 = U_0$ have been used. The identities follow from the conditions at the initiation of decohesion that $\bar{u} = 0$ and $\tau^{**} = 1$.

We note that the decohesion condition ($F_d^* = 0$) reduces to $\tau^{**} = 1 - \bar{\tau}^*$. As decohesion occurs \bar{u} increases and τ^{**} decreases to zero when $\bar{u} = \bar{u}_0$. Therefore \bar{u}_0 can be interpreted as the value of \bar{u} at which separation occurs. In the post separation regime, $\bar{u} > \bar{u}_0$, the decohesion condition is $\tau^{**} = 0$. Finally, we give an alternative form for the decohesion evolution function:

$$\mathbf{m}^* = \frac{U_0}{\tau^{**}} \left(\frac{\tau_n}{\tau_{nf}^2} \mathbf{n} + \frac{\tau_t}{\tau_{tf}^2} \mathbf{t} \right) \quad (24)$$

Since the dissipation rate is $\dot{\lambda} U_0$, the energy dissipated per unit surface area at any moment is simply λU_0 . From (20), $\lambda = 1$ at separation so the maximum energy dissipated is U_0 which provides a physical interpretation and a method for determining this particular parameter. The formulation implies the dissipated energy is independent of path which is generally not representative of real materials. The final value of the stored energy is obtained by substituting $\bar{u} = \bar{u}_0$ in (19) and using (16). In summary, the final dissipated, stored and total failure energies are:

$$\Phi_D = U_0 \quad \Phi_U = -\frac{1}{(q+1)} U_0 \quad \Phi_F = \frac{q}{(q+1)} U_0 \quad (25)$$

Suppose a pure opening-mode path is followed, or $\tau_t = 0$. Then it is easily shown that $u_n = \bar{u}(\bar{\tau}_0 / \tau_{nf})$. If $\bar{\tau}_0$ is chosen to equal τ_{nf} , then \bar{u} equals u_n for Mode I. Experimental data obtained from a pure shear mode test can then be used to

assess the adequacy of the model in a process similar to that used to evaluate Mises plasticity. The limitation of a single value of dissipated energy can be circumvented by using a multifunctioned decohesion surface. The development of such a surface is beyond the scope of what we wish to achieve. For the given model, the required data are τ_{nf} , τ_{tf} , U_0 and q . We can choose $\bar{\tau}_0 = \tau_{nf}$ and then $\bar{u}_0 = U_0 / \tau_{nf}$ to provide values for all of the parameters.

Sometimes nonassociated models are required to provide a better fit with experimental data including observations on the mode of failure. Next we give an example of how a particular nonassociated model can be constructed.

3.3 Model 2: Nonassociated Evolution Functions

Suppose we retain all aspects of the previous model with the exception that the evolution equation for the permanent decohesion is in the normal, or opening, direction irrespective of the state of traction:

$$\dot{u}_n^p = \dot{\lambda} m_n^c \quad \dot{u}_t^p = 0 \quad m_n^c = \mathbf{m}^c \cdot \mathbf{n} \quad (26)$$

We retain the previous expression for τ^c and the decohesion function. Therefore, the dissipation rate for normal mode decohesion must be evaluated specifically from the following equation:

$$D_{t,n} = \tau \cdot \dot{\mathbf{u}}^p + \bar{\tau} \dot{\bar{u}} = \dot{\lambda} [\tau_n \dot{u}_n^p + \bar{\tau} \bar{u}_0] \quad (27)$$

which will be less than that obtained with the associated rule (sometimes called the Principle of Maximum Dissipation) if τ_t is not zero for at least part of the decohesion.

A corresponding development for Mode II (pure shear) evolution can be obtained by merely replacing normal components of traction with shear components.

4. Numerical Application

4.1 Incorporation with the Material Point Method

In general, there is no need to determine the actual shape of the deformed material element associated with each material point. However, when material separation occurs, there is a need to consider the effect on the strain field over the material element (compatibility). For small deformations, which would be the case normally for quasibrittle materials and for small rotations, the original configuration can be used. Typically, each cell with the material point method is chosen to be a square element with each side of length h and the element associated with each material point can also be chosen similarly to be a square of size $h_p = h / \sqrt{n_p}$ where n_p is the number of material points per cell. Over each material element, the increment in strain, $\Delta \mathbf{e}$, is assumed to be constant as is the increment in decohesion, $\Delta \mathbf{u}^d$, as indicated in Fig. 4 which also shows the unit vector $\mathbf{m} = \Delta \mathbf{u}^d / |\Delta \mathbf{u}^d|$. For future use, define the opening, M_n , shear, M_p , and failure, M_m , tensor modes as follows:

$$\mathbf{M}_n = \mathbf{n} \otimes \mathbf{n} \quad \mathbf{M}_t = \frac{1}{2}(\mathbf{n} \otimes \mathbf{t} + \mathbf{t} \otimes \mathbf{n}) \quad \mathbf{M}_m = \frac{1}{2}(\mathbf{n} \otimes \mathbf{m} + \mathbf{m} \otimes \mathbf{n}) \quad (28)$$

We note that \mathbf{M}_m reduces to \mathbf{M}_n and \mathbf{M}_t when $\mathbf{m} = \mathbf{n}$ and $\mathbf{m} = \mathbf{t}$, respectively.

For a given time increment, if the total (average) strain increment, $\Delta \mathbf{e}$, is considered fixed, the result of the decohesion is that the effective strain increment in the remaining part of the material in the element must be reduced (relaxed) by what might be called a decohesion strain increment, $\Delta \mathbf{e}^d$, which satisfies a weak form of the compatibility condition

$$\int_{\Omega_p} \Delta \mathbf{e}^d dV = \int_{\partial\Omega_d} \Delta u^d \mathbf{M}_m dA \quad \Delta \mathbf{u}^d = \Delta u^d \mathbf{m} \quad (29)$$

in which dV and dA denote differentials of volume on the material element, Ω_p , and of area on the decohesion surface, $\partial\Omega_d$, respectively. The magnitude of the decohesion increment, which is in the direction of \mathbf{m} by definition, is Δu^d . With the assumptions that the decohesion and strain are constant over each material element, the result is the following expression relating the “relaxation” or “decohesion” strain increment to the increment in decohesion:

$$\Delta \mathbf{e}^d = \frac{\Delta u^d}{L_e} \mathbf{M}_m \quad L_e = \frac{V_p}{A_d} \quad (30)$$

The effective length, L_e , is merely the ratio of the element volume to the area of the decohesion surface within that element. For the two-dimensional case illustrated in Fig. 2, the effective length is

$$L_e = \frac{h_p}{\cos \alpha_p} \quad 0 \leq \alpha_p \leq \frac{\pi}{4} \quad (31)$$

with a corresponding formula for an angle measured with respect to the other side of the material element if $\alpha_p > \pi/4$.

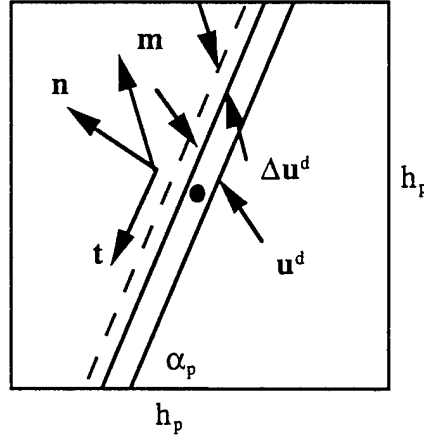


Fig. 2. A typical material element with decohesion.

4.2 Solution Algorithm

The constitutive equations subroutine is invoked with the total strain increment, $\Delta \mathbf{e}$, prescribed, with the total decohesion equal to the plastic decohesion, and with \mathbf{n} given and assumed fixed. It is computationally more efficient to define an alternative mode vector, \mathbf{m}^* , from which the mode vector, \mathbf{m}^e , and an alternative tensor mode, \mathbf{M}^* , are easily determined. Let $\boldsymbol{\sigma}_p$, \mathbf{u}_p and λ_p denote the values of $\boldsymbol{\sigma}$, \mathbf{u}^p and λ , respectively, at the end of the previous step. The requirement is to solve the following set of nonlinear equations:

$$\begin{aligned}
 \Delta \boldsymbol{\sigma} &= \Delta \boldsymbol{\sigma}^e - \mathbf{E} : \Delta \mathbf{e}^d & \Delta \boldsymbol{\sigma}^e &= \mathbf{E} : \Delta \mathbf{e} \\
 \boldsymbol{\tau}_p &= \boldsymbol{\sigma}_p \cdot \mathbf{n} & \Delta \boldsymbol{\tau}^e &= \Delta \boldsymbol{\sigma}^e \cdot \mathbf{n} \\
 \mathbf{m}^* &= \frac{\mathbf{A}_d \cdot \boldsymbol{\tau}}{\bar{\tau}_0 \tau^{e*}} & \mathbf{m}^e &= \bar{u}_0 \mathbf{m}^* \\
 \boldsymbol{\sigma}_m &= \mathbf{E} : \mathbf{M}^* & \boldsymbol{\tau}_m &= \boldsymbol{\sigma}_m \cdot \mathbf{n} \\
 \Delta \mathbf{e}^d &= \Delta \lambda \mathbf{M}^* & \Delta \mathbf{u}^p &= \Delta \lambda \mathbf{m}^e \\
 \Delta \boldsymbol{\tau} &= \Delta \boldsymbol{\tau}^e - \Delta \lambda \boldsymbol{\tau}_m & \boldsymbol{\tau} &= \boldsymbol{\tau}_p + \Delta \boldsymbol{\tau} \\
 \mathbf{u}^p &= \mathbf{u}_p + \Delta \mathbf{u}^p & \lambda &= \lambda_p + \Delta \lambda \\
 \bar{\tau}^* &= \lambda^q & \tau^{e*} &= \left(\frac{\boldsymbol{\tau} \cdot \mathbf{A}_d \cdot \boldsymbol{\tau}}{\bar{\tau}_0} \right)^{1/2} \\
 \mathbf{M}^* &= \frac{1}{2} \frac{\bar{u}_0}{L_c} (\mathbf{n} \otimes \mathbf{m}^* + \mathbf{m}^* \otimes \mathbf{n}) \\
 F_d^* &\equiv \tau^{e*} - (1 - \bar{\tau}^*) = 0 \\
 \boldsymbol{\sigma} &= \boldsymbol{\sigma}^e - \Delta \lambda \boldsymbol{\sigma}_m
 \end{aligned} \tag{32}$$

The first step is to assume that no decohesion occurs, to obtain a trial stress and traction:

$$\boldsymbol{\sigma}^e = \boldsymbol{\sigma}_p + \Delta \boldsymbol{\sigma}^e \quad \boldsymbol{\tau}^e = \boldsymbol{\sigma}^e \cdot \mathbf{n} \tag{33}$$

and then determine the value of the damage function, F_d^{tr} , for this trial traction and the existing value λ_p . If $F_d^{tr} \leq \epsilon$ the step is purely elastic with no additional decohesion and no further action is required. If the inequality is not satisfied, the decohesion variables must be incremented.

Next we describe a one-step algorithm which enforces the requirement $F_d = 0$ to order $(\Delta \lambda)^3$. Perform a Taylor expansion of F_d about the trial state:

$$F_d = a(\Delta \lambda)^2 + 2b\Delta \lambda + c + O(\Delta \lambda)^3 \tag{34}$$

in which the last term indicates the order of the remainder and

$$a = \frac{1}{2} \frac{\partial^2 F_d}{\partial \lambda^2} \Big|_{tr} \quad 2b = \frac{\partial F_d}{\partial \lambda} \Big|_{tr} \quad c = F_d^{tr} \tag{35}$$

We choose $\Delta \lambda = \Delta \lambda_1$ and $\Delta \lambda = \Delta \lambda_2$ to be the solutions to the first-order and second-order equations, respectively; i.e., $2b\Delta \lambda_1 + c = 0$ and $a(\Delta \lambda_2)^2 + 2b\Delta \lambda_2 + c = 0$ or

$$\Delta \lambda_1 = -\frac{c}{2b} \quad \Delta \lambda_2 = \frac{-b \pm \sqrt{b^2 - ac}}{a} \tag{36}$$

with the sign chosen so that in the limit of infinitesimal $\Delta \lambda$ we have $\Delta \lambda_2 = \Delta \lambda_1$.

Consider the case when the model choice of (20) is used and the Taylor expansion is applied to the dimensionless damage function F_d^* . It follows from (35) that

$$c = (\tau^{**})^q - (1 - \lambda_{pr}^q)$$

$$2b = \frac{\partial \tau^{**}}{\partial \tau} \cdot \frac{\partial \tau}{\partial \lambda} + q \lambda_{pr}^{q-1} \quad (37)$$

$$2a = \frac{\partial \tau}{\partial \lambda} \cdot \frac{\partial^2 \tau^{**}}{\partial \tau^2} \cdot \frac{\partial \tau}{\partial \lambda} + \frac{\partial \tau^{**}}{\partial \tau} \cdot \frac{\partial^2 \tau}{\partial \lambda^2} + q(q-1) \lambda_{pr}^{q-2}$$

in which all terms are to be evaluated at λ_{pr} and the trial value of the traction. Note that when $q = 1$, the last term in the expression for a is zero. With a modest amount of algebra involving (32), it follows that

$$\frac{\partial \tau}{\partial \lambda} = -\tau_m \quad \frac{\partial \tau^{**}}{\partial \tau} = \frac{\mathbf{m}^*}{\tau_0} \quad (38)$$

and we immediately have the relation

$$2b = -\frac{\mathbf{m}^* \cdot \tau_m}{\tau_0} + q \lambda_{pr}^{q-1} \quad (39)$$

Next, we proceed to obtain the coefficient a in (37). We utilize (32) and (38) to obtain

$$\frac{\partial^2 \tau^{**}}{\partial \tau^2} = \frac{1}{\tau_0^2 \tau^{**}} [\mathbf{A}_d - \mathbf{m}^* \otimes \mathbf{m}^*] \quad (40)$$

which leads to

$$\frac{\partial \tau}{\partial \lambda} \cdot \frac{\partial^2 \tau^{**}}{\partial \tau^2} \cdot \frac{\partial \tau}{\partial \lambda} = \frac{[(\tau_m \cdot \mathbf{A}_d \cdot \tau_m) - (\tau_m \cdot \mathbf{m}^*)^2]}{\tau_0^2 \tau^{**}} \quad (41)$$

Finally

$$\frac{\partial^2 \tau}{\partial \lambda^2} = -\frac{\partial \tau_m}{\partial \lambda} = -\mathbf{n} \cdot \mathbf{E} : \frac{\partial \mathbf{M}^*}{\partial \lambda} = -\mathbf{n} \cdot \mathbf{E} : \frac{\bar{\mathbf{u}}_0}{L_c} (\mathbf{n} \otimes \frac{\partial \mathbf{m}^*}{\partial \lambda}) \quad (42)$$

in which the minor symmetry of \mathbf{E} has been used. We note that

$$\frac{\partial \mathbf{m}^*}{\partial \lambda} = \frac{\partial \mathbf{m}^*}{\partial \tau} \cdot \frac{\partial \tau}{\partial \lambda} = -\frac{1}{\tau_0} \frac{\partial^2 \tau^{**}}{\partial \tau^2} \cdot \tau_m = -\frac{1}{\tau_0} [\mathbf{A}_d - \mathbf{m}^* \otimes \mathbf{m}^*] \cdot \tau_m \quad (43)$$

$$\frac{\partial \tau^{**}}{\partial \tau} \cdot (-\mathbf{n} \cdot \mathbf{E} : \frac{\bar{\mathbf{u}}_0}{L_c} \mathbf{n}) = -\frac{1}{\tau_0} (\mathbf{m}^* \otimes \mathbf{n}) : \mathbf{E} : \frac{\bar{\mathbf{u}}_0}{L_c} \mathbf{n} = -\frac{\tau_m}{\tau_0}$$

with the result

$$\frac{\partial \tau^{**}}{\partial \tau} \cdot \frac{\partial^2 \tau}{\partial \lambda^2} = \frac{[(\tau_m \cdot \mathbf{A}_d \cdot \tau_m) - (\tau_m \cdot \mathbf{m}^*)^2]}{\tau_0^2 \tau^{**}} \quad (44)$$

a result identical to that of (41). Therefore

$$a = \frac{[(\tau_m \cdot \mathbf{A}_d \cdot \tau_m) - (\tau_m \cdot \mathbf{m}^*)^2]}{\tau_0^2 \tau^{**}} + \frac{q(q-1)}{2} \lambda_{pr}^{q-2} \quad (45)$$

Even with this rather simple form, preliminary numerical results indicate that the use of the first-order equation for $\Delta \lambda_1$ in (36) is sufficiently accurate and the extra computations required to get a is not justified.

4.3 Separation

The procedure outlined above holds until separation occurs as indicated by $\lambda \geq 1$. The given algorithm can be used also for separation with the revised damage function $F_d^* = \tau^{**}$ so that $F_d^* = 0$ enforces the separation condition that $\tau = 0$ and $\Delta \tau = 0$. To

prevent the possibility of numerical problems when F_d^* is close to zero, the decohesion criterion is applied for $F_d^* \geq \epsilon$ and the separation condition is used when $F_d^* < \epsilon$ where ϵ is a small positive number (typically 0.01). The value of the stress component, $\sigma_n = \mathbf{t} \cdot \boldsymbol{\sigma} \cdot \mathbf{t}$, is automatically adjusted through the equilibrium equations.

4.4 Example Solution

The application given in this section is restricted to a case for which (i) the initiation of failure is given directly by a failure criterion rather than by a discontinuous bifurcation analysis, and (ii) the orientations of the surfaces of decohesion are known, *a priori*. The purpose of these numerical analyses is: (a) To illustrate that the use of jump in displacement as an internal variable together with a weak implementation of compatibility provides a simple and useful algorithm in the MPM, (b) to show that the MPM does not exhibit the finite element pathologies associated with distorted meshes and instabilities with the result that additional features such as enhanced strains are not required, and (c) to illustrate by example that the material point method does not exhibit the orientation effect often seen with finite elements when discontinuities are allowed to propagate at various angles to the mesh sides.

In this example a material composed of grains with isotropic elastic properties but anisotropic thermal properties is cooled from room temperature (20° C) to -50° C, at which point the temperature is held fixed. The cooling rate is -10° C/ μ s. The coefficient of thermal expansion is $2.25 \times 10^{-4}/^\circ\text{C}$ along the 1-1 material axis of each grain but an order of magnitude smaller, $2.1 \times 10^{-5}/^\circ\text{C}$, along the 2-2 material axis. Several grains of this material are made into a composite material where the grains are assembled into the composite with random orientation.

Figure 3 shows a 1 mm square sample of grains marked by material points. An arrow indicates the 1-1 material direction of each grain. The grains have isotropic elastic properties, with a Young's modulus 3.28 GPa, Poisson's ratio 0.3, and density 1.9 kg/m³. The interstitial region has the same material properties and is also represented by material points (Fig. 4), however, these points are allowed to follow a non-associated decohesion constitutive model in which the mode is normal to the grain boundary. The decohesion constitutive properties are as follows: the peak normal traction is $\tau_{nt} = 5.5$ MPa, $q = 1$, and $U_0 = 0.055$ J/m². The peak stress in shear was not required because of the nonassociated evolution equation.

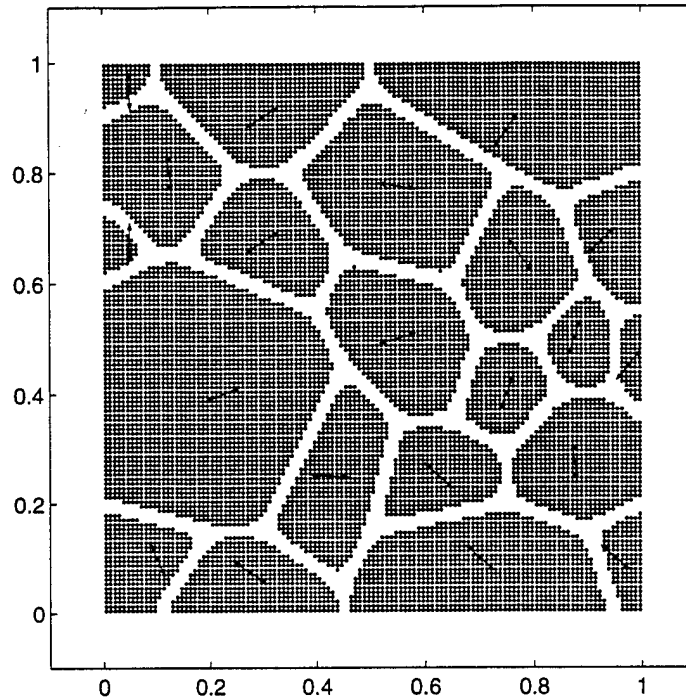


Fig. 3. Sample of anisotropic grains with the direction of the 1-1 material axis indicated with an arrow

The normal to a grain boundary is computed by assigning a scalar color, with the value one, to the material points making up the grain, interpolating that color to the background mesh and then taking the gradient. The gradient gives the inward normal to the grain. Figure 5 shows an example of the computed normals for a grain. The computational mesh is square with side length of 25 microns.

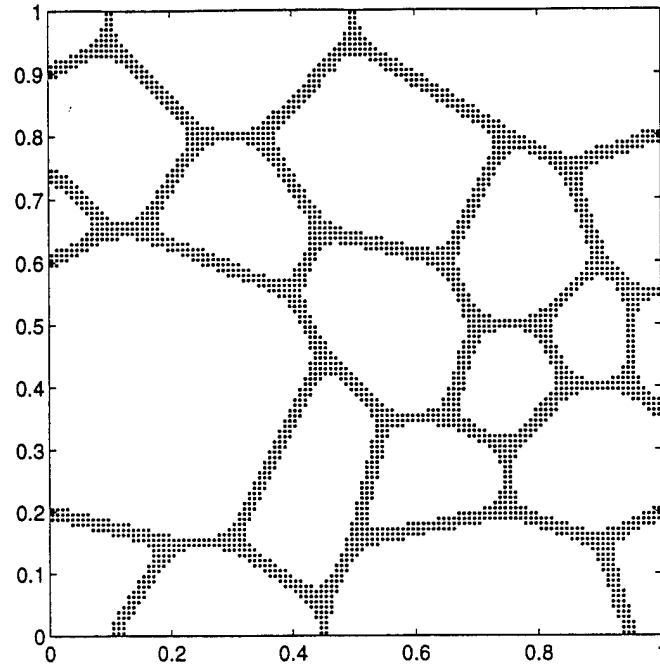


Fig. 4. Interstitial region is also discretized using material points.

As the material cools, the anisotropic thermal properties cause the contraction to be nonuniform. The effect of the variability in the stress field is seen in Fig. 6 where contours of the jump in displacement are shown at various times. Decohesion starts in the upper right quadrant of the sample, and the location of the initial decohesion has the largest value throughout the computation. However, the decohesion does not propagate from the maximum all the way across the domain, instead a different path on the left side of the sample seems more likely to span the domain. This calculation indicates the complex interaction of geometry and material properties that make predicting the path of crack propagation so difficult.

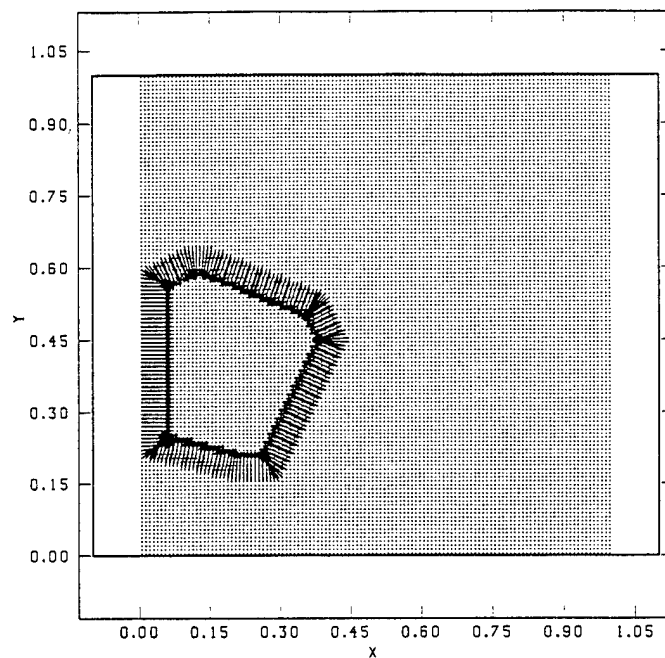


Fig. 5. The normal to the boundary is computed by taking the gradient of the color function.

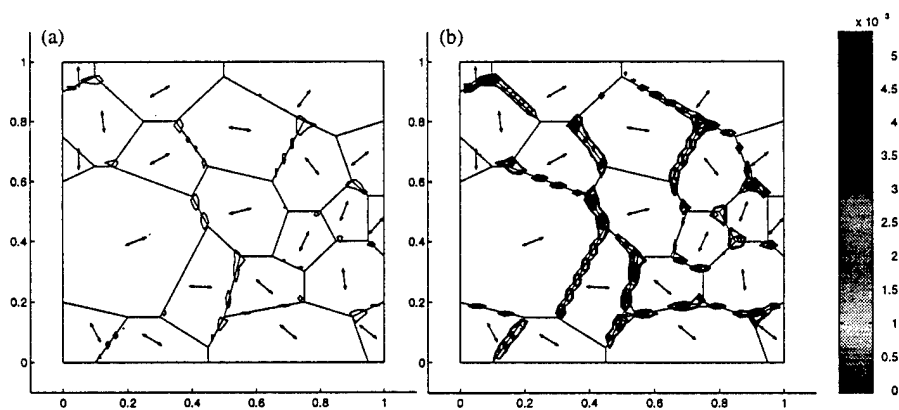


Fig. 6. Grayscale contour plot of the jump in displacement at time (a) $2\mu\text{s}$ and (b) $5\mu\text{s}$.

5. SUMMARY

A rigid, plastically softening decohesion model has been combined with continuum elasticity and traction continuity at a material failure surface to provide a relatively simple description for the evolution of material failure. When incorporated in the material point method, the result is a constitutive equation subroutine that is similar to softening plasticity. A length parameter associated with a material element provides a mechanism for ensuring convergence with mesh refinement. As the tip of a failure surface propagates through the mesh, the formulation inherent with the material point method appears to preclude the diffusion of the crack tip, a feature often seen with conventional finite elements. Further investigations involving the propagation of curved cracks is necessary to determine whether or not the proposed method is general and robust. Nevertheless, in light of the long history of complex numerical analysis in connection with crack propagation, we believe the simplicity of the decohesion formulation in the material point method holds considerable promise for development into a general method for predicting material failure.

6. ACKNOWLEDGMENT

This work was partially supported at various times by Los Alamos National Laboratory, Sandia National Laboratories and the Air Force Office of Scientific Research

7. REFERENCES

- [All 95] ALLIX, O., ET AL. , "Damage analysis of interlaminar fracture specimens," *Composite Structures*, VOL. 31, p. 61-74, 1995.
- [ALL 96] ALLIX, O., CORIGLIANO, A., "Modeling and simulation of crack propagation in mixed-modes interlaminar fracture specimens," *International Journal of Fracture*, vol. 77, p. 111-140, 1996.
- [ARM 97] ARMERO, F., "Large-scale modeling of localized dissipative mechanisms in a local continuum: applications to the numerical simulation of strain localization in rate-dependent inelastic solids," to appear in *Mechanics of Cohesive-Frictional Materials*, 1997.
- [BAR 59] BARENBLATT, G.I., "The formation of equilibrium cracks during brittle fracture; general ideas and hypotheses: axially symmetric cracks," *J. Appl. Math. Mech.*, vol. 23, p. 622-636, 1959.
- [BAZ 83] BAZANT, Z.P., OH, B.H., "Crack band theory for fracture of concrete," *Materials and Structures RILEM*, vol. 16, p. 155-177, 1983.

- [BAZ 97] BAZANT, Z.P., LI, L.N., "Cohesive crack with rate-dependent opening and viscoelasticity - I - mathematical model and scaling; -II - numerical algorithm, behavior and size effect," *Int. J. of Fracture*, vol. 86(3), p. 247-266 and 267- 279, 1997.
- [BOR 87] BORST, R. de, , "Smeared cracking, plasticity, creep and thermal loading - a unified approach," *Computational Methods in Appl. Mech. Engrg.*, vol. 72, p. 89-110, 1987
- [DAH 90] DAHLBOM, O., OTTOSEN, N.S., "Smeared crack analysis using generalized fictitious crack model," *J. of Engineering Mechanics*, vol. 116, p. 55-76, 1990.
- [COR 93] CORIGLIANO, A., , "Formulation, identification and use of interface models in the numerical analysis of composite delamination," *Int. J. Solids Structures*, vol. 30(20), p. 2779-2811, 1993.
- [DVO 90] DVORKIN, E. et al., "Finite Elements with Displacement Interpolated Embedded Localization Lines Insensitive to Mesh Size and Distortions," *Int. J. for Num. Methods in Eng.*, vol. 30, p. 541-564, 1990.
- [FEE 91a, 91b] FEENSTRA, P.H., et al., "Numerical Study of Crack Dilatancy. I: Models and Stability Analysis," and "II: Applications" *J. of Engineering Mechanics*, vol. 117, p. 733-753 and p. 754-769, 1991.
- [HIL 76] HILLERBORG, A., et al., "Analysis of Crack Formation and Crack Growth in Concrete by Means of Fracture Mechanics and Finite Elements," *Cement and Concrete Research*, vol. 6, p. 773-782, 1976.
- [LAR 96] LARSSON, R., and RUNESSON, K., "Element-embedded localization band based on regularized displacement discontinuity," *J. of Engineering Mechanics*, vol. 122(5), p. 402-411, 1996.
- [OLI 89] OLIVER, J., "A consistent characteristic length for smeared cracking problems," *Int. J. Num. Meth. Eng.*, vol. 28, p. 461-474, 1989.
- [OLI 96a, 96b] OLIVER, J., "Modelling Strong Discontinuities in Solid Mechanics via Strain Softening Constitutive Equations. Part 1: Fundamentals," and "Part 2: Numerical Simulations," *Int. J. for Num. Methods in Eng.*, vol. 39, p. 3575-3600 and p. 3601-3623, 1996
- [NEE 87] NEEDLEMAN, A., "A continuum model for void nucleation by inclusion debonding," *J. of Applied Mechanics*, vol. 54, p. 525-531, 1987
- [ROT 87] ROTS, J.G., and de BORST, R., "Analysis of mixed-mode fracture in concrete," *J. of Engineering Mechanics*, vol. 113, p. 1739-1758, 1987.
- [SCH 92] SCHELLEKENS, J.C.J., *Computational Strategies for Composite Structures*, Ph.D. Dissertation, Dept. of Civil Engineering, The Delft University of Technology, Delft, The Netherlands, 1992.
- [SIM 93] SIMO, J.C., et al., "An analysis of strong discontinuities induced by strain-softening in rate-independent solids," *Computational Mech.*, vol. 12, p. 277-296, 1993.
- [SIM 94] SIMO, J.C., OLIVER, J., "A new approach to the analysis and simulation of strain-softening in solids," *Fracture and Damage in quasi-Brittle Materials*, ed. by Z.P. Bazant et al., Workshop held in Prague, 1994
- [SUO 92] SUO, Z., et al., "Stability of Solids with Interfaces," *J. Mech. Phys. Solids*, Vol. 40, No. 1, 613-640, 1992.

- [SUL 94] SULSKY, D., et al., "A Particle Method for History-Dependent Materials," *Computer Methods in Applied Mechs. and Engineering*, vol. 118, p. 179-196, 1994.
- [SUL 95] SULSKY, D., et al., "Application of a Particle-in-Cell Method to Solid Mechanics," *Computer Physics Communications*, vol. 87(1&2), p. 236-252, 1995.
- [SUL 96] SULSKY, D., SCHREYER, H.L., "Axisymmetric Form of the Material Point Method with Applications to Upsetting and Taylor Impact Problems," *Comp. Methods in Applied Mechanics & Eng.*, vol. 139(1-4), p. 409-429, 1996.
- [WIE 98] WIEHE, S., et al., "Classification of smeared crack models based on material and structural properties," *Int. J. Solids Structures*, vol. 35(12), p. 1289-1312, 1998.
- [ZHO 98] ZHOU, S., *The Numerical Prediction of Material Failure Based on the Material Point Method*, Ph.D. Dissertation, Department of Mechanical Engineering, The University of New Mexico, Albuquerque, NM, 1998.

EXPERIMENTAL AND NUMERICAL INVESTIGATIONS OF CONCRETE FAILURE UNDER TRIAXIAL LOADING

Ming L. Wang, and Zhenlei Chen
Department of Civil and Materials Engineering
University of Illinois at Chicago
Chicago, IL 60607
U.S.A.

Abstract

Experimental and numerical simulations are presented in order to define the failure mechanism of cementitious materials.

Triaxial tests on 95 mortar cylinders show there is a change in the failure plane orientation as confining pressure increases. The failure is characterized by a distinct failure surface or surfaces that change orientation from nearly vertical to angled as confinement increases. Cap blocks are used to relieve the friction between the platens and the specimens under triaxial loading. The same conclusion is obtained by numerical analysis that includes a realistic 3-dimensional meso-structure simulation. A modified Gauss point method is applied to guarantee the efficiency and accuracy of the finite element analyses. The Drucker-Prager criterion and the low tensile strength criterion are used to simulate the failure mechanism.

Key words: Triaxial test, random aggregate distribution, modified Gauss point, failure mechanisms

1 Introduction

Triaxial tests have shown that the angle of the failure plane for geologic materials changes with increasing confining pressure (Wawersik, 1971; Murrell, 1965). However, no detailed data for concrete has shown that there is a similar relationship between the confinement and the change in the angle of the principle failure plane. Palaniswamy (1972), commenting on triaxial tests

on cement paste, mortar, and concrete, stated that two distinct modes of behavior were observed, specifically, a splitting failure at low confining pressures, and a crushing failure at large confining pressures. Zimmerman (1977) found that the failure plane is always parallel to the direction of maximum compressive stress. The apparatus used in his tests employed platens to apply lateral pressure to the specimens. These platens may have constrained the true failure modes of the specimens. Tests by Gerstle (1980), using several different loading devices, showed that boundary constraints from the use of platens for lateral loading inhibit transverse deformations.

In this paper, both experimental and numerical studies show changes in the orientation of the failure plane as confining pressure increases.

Experimentally, it is essential to relieve the friction between the platens since this friction severely affects the development of the failure mechanism and, consequently, its orientation. Moreover the failure is characterized by a distinct failure surface or surfaces that change orientation from nearly vertical to angled as confinement increases. The same conclusion is obtained by numerical analysis that includes a realistic 3-dimensional meso-structure simulation. A modified Gauss point method is applied to guarantee the efficiency and accuracy of the huge-scale finite element analyses (148,500 lattices). Based on comparison of the experimental and numerical results, the strength ratio between cement paste (including interface) and coarse aggregate is randomly distributed between 0.1 to 0.4. The Drucker-Prager criterion and the low tensile strength criterion are used to simulate the failure mechanism.

2 Experimental Technique

Triaxial tests were performed with confining pressures ranging from 0 to 56 Mpa. A total of 95 cylinders were tested in triaxial compression. Evaluating the effect of the methods used to relieve friction between the load platens and the specimens was essential in this study.

2.1 Equipment Setup

A behavioral science engineering laboratories 70 kpa triaxial test cell was used to apply the lateral confining pressure. The test cell had a pressure transducer that was used to monitor fluid pressure inside the cell. The axial load was applied with a universal testing machine.

Measurements Group, Inc., EA-06-500BL-350 strain gauges were used in 56% of the tests (Wang and Ruthland, 1995). Only load-displacement data were recorded in the remaining tests. Axial load and displacement data were recorded on an X-Y plotter. Some of the test data were digitized and stored on an IBM-compatible personal computer using an analog to digital converter.

2.2 Specimen Preparation

All triaxial specimens were prepared with a water/cement ratio between .42 and .47. The cement/aggregate ratio was .25 by weight. Superplasticizer, Frizpak Supercizer 6, was added to increase the workability of the mixes .3% by weight of cement.

Seventy-five specimens measuring 5 cm in diameter by 10 cm in height were cast in three batches of 25. Twelve specimens 5 cm in diameter by 20 cm in height were cast in a separate batch.

Cap blocks were prepared to help relieve the friction between the platens and the specimens. The cap blocks were 5 cm in diameter and 1.3 to 2.5 cm thick. The mix design for the cap blocks was similar to that of the specimens except that the cement/aggregate ratio was increased to .4, the water/cement ratio was decreased to .35, and the amount of superplasticizer was increased to .5%. The goal was to produce a material with similar deformation properties but with a higher strength. The modulus and lateral extension ratio of the two materials were similar (within 5%), while the uniaxial strength of the cap blocks was 50% larger than the strength of the specimens.

All specimen and cap blocks were polished on a lap table containing a coarse grit (100) lap pad. The cylinders and cap blocks contained air voids on the surfaces that would tear the triaxial membranes. In order to protect the membranes the surface voids were filled with clay. Triaxial membranes were placed on the specimens.

Several methods of relieving the friction between the specimen and the platens were tested. Based on some preparing tests, cap blocks alone, cap blocks with grease, and cap blocks with polyethylene sheets, were used to relieve the friction. All the tests were performed at 0, 1.7, 3.5, 7.0, 14.0, 28.0, 42.0, and 56.0 Mpa, and they were conducted using a standard triaxial loading where the displacement was monotonically increased up to and past the peak load.

3 Mesostructure Simulation

In meso- or micro-scopic studies, it is necessary to generate a realistic 3-

dimensional multiphase system consisting of cement paste and coarse aggregate, especially for concrete (Desiderio, 1996). This is because mechanical behaviors are determined by extremes in the local stresses, which have a close relationship with the distribution of cement pastes and coarse aggregates, as well as with aggregate sizes in the meso-structure simulation. Here, the Monte Carlo method (Hassold, 1996) is used to simulate the cylinder specimen measuring 5 cm in diameter and 10 cm in height.

Automatic mesh generation produced 148,500 lattices for the cylinder sample (Fig. 1). Generally, that amount of lattices is necessary to reach a properly aggregated size of the given concrete specimen. A non-zero index, which corresponds to both the phase and orientation of the aggregate, is initialized to each lattice by a random function. In a 2-phase simulation (α and β), the sign of S_i indicates the phase present at that site, while the absolute value of S_i corresponds to the orientation of the grain in which the site is embedded. Sites with one or more different closest neighbors are interface sites, sites with only like nearest neighbors are interior sites. Total system energy is specified by assigning a positive energy to interface areas (or cement pastes) and zero energy to the interior sites (or coarse aggregates), which can be calculated via the Hamiltonian equation (Hockin, 1980)

$$H = \frac{1}{8} \sum_{i=1}^N \sum_{j=1}^Z \left\{ (J_{\alpha\alpha} + J_{\beta\beta} + 2J_{\alpha\beta})[1 - \delta(S_i, S_j)] + (J_{\alpha\alpha} + J_{\beta\beta} - 2J_{\alpha\beta}) \right. \\ \left. \text{Sign}(S_i)\text{Sign}(S_j) + (J_{\alpha\alpha} - J_{\beta\beta})[\text{Sign}(S_i) + \text{Sign}(S_j)] \right\} \quad (1)$$

In equation (1), N is the total sites of system. Z is the number of neighbors of i^{th} site. δ is the Kronecker delta function. 'Sign' is the sign function defined as $\text{Sign}(S_i)$ equals 1 if S_i is positive, and $\text{Sign}(S_i)$ equals -1 if S_i is negative. $J_{\alpha\alpha}$, $J_{\beta\beta}$ and $J_{\alpha\beta}$ are α - α , β - β , and α - β interfacial energies, respectively.

In iteration, the kinetic energy of the aggregate is adjusted by the Monte Carlo technique. First, a lattice site and a site index are chosen at random. The index of the chosen site is then changed to the new index if the corresponding total system energy, H , does not increase. After each attempted index change, the Monte Carlo step increases, and a simulated mesostructure is yielded. Fig. 2 is a 3-dimensional simulated mesostructure plot of the cylinder specimen that involves 148,500 lattices. Different types of aggregates are composed of certain numbers of lattices, and between the aggregates are the interfaces or cement pastes.

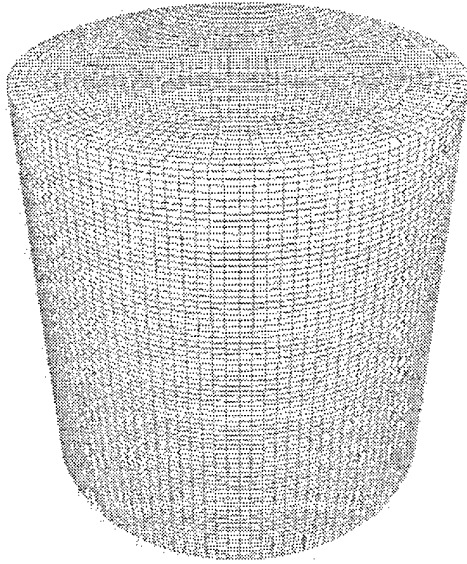


Fig.1 Specimen lattice Plot



Fig.2 Specimen aggregate distribution

4 Model Description

Simulations of the static tests were performed using the finite element analysis code, which was developed for static analysis of nonlinear structural systems. The Drucker-Prager criterion and the low tensile strength criterion are used. Based on comparison of the experimental and numerical results, the strength ratio between the cement paste (including interface) and coarse aggregate was randomly distributed between 0.1 to 0.4. Table 1 is the parameter used in the analysis.

Table 1 Parameters for coarse aggregate*

Young's Modulus	Poisson's Ratio	Maxi. Tensile Stress	Maxi. Comp-ressive Stress	Cohesion
17 MPa	0.167	20 MPa	100 Mpa	22.4 MPa

*Strength ratio between cement paste (including interface) and aggregate: 0.1~0.4 randomly.

An 8-node isoparameter 3-dimensional element was used. In this case, there were 148,500 lattices in the cylinder model and each of them possessed different mechanical properties, such as ultimate strength and modulus of elasticity, which need to be incorporated in numerical analyses. However, it is very difficult or almost impossible to treat that many elements in finite element analysis due to the low efficiency and floating point errors of the

calculation. The situation becomes even more difficult with nonlinear analysis.

Modified Gauss point method has been successfully used to reduce the computer processing time while still guaranteeing accuracy (Wang and Chen, 1997). The basic idea of the modified Gauss point method used here is that each Gauss point in the numerical integration corresponds to one lattice and, therefore, one element will involve a specific number of lattices, say 8 or 27 in a 3-dimensional problem. The Gauss point coordinates and the corresponding weight coefficients need to be modified because of the evenly distributed lattices. Table 2 lists the values of Gauss point coordinates, ξ_i , and the weighted coefficient, H_i , for the different number of Gauss points, n , evenly distributed between -1 and $+1$ in case of 1-dimensional.

Table 2 Values of ξ_i corresponding to various n

n	H_i	ξ_i	Precise for m^{th} Order Polynomial
3	2/3	± 0.707107 0.0	$m=3$
4	2/4	± 0.794654 ± 0.187593	$m=4$ or 5
5	2/5	± 0.832497 0.0 ± 0.374541	$m=5$
6	2/6	± 0.866246 ± 0.422522 ± 0.374541	$m=5$ or 6

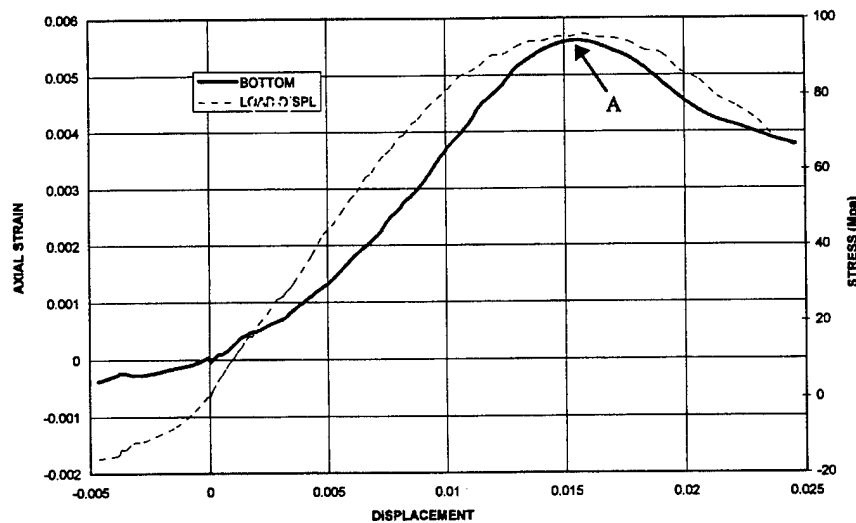


Fig.3(a) Typical displacement-stress relationship of experimental data (Units of displacement is in cm)

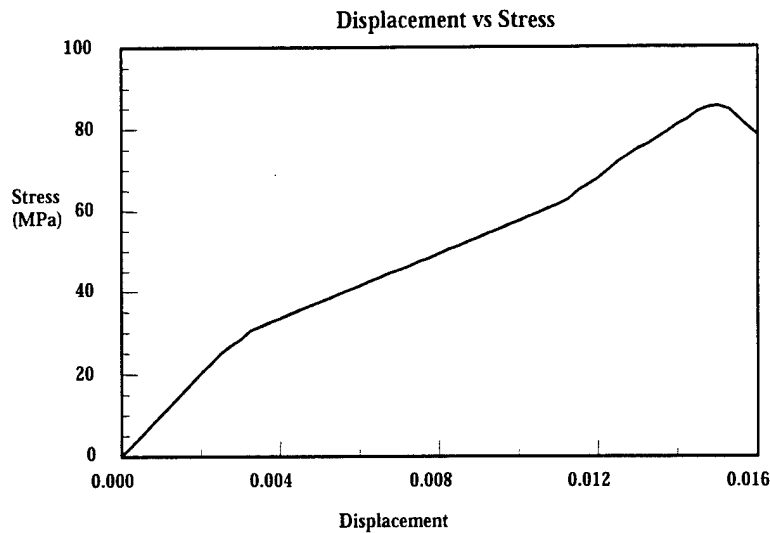


Fig.3(b) Typical displacement-stress relationship Numerical simulation (Units of displacement is in cm)

In this paper, 27 modified Gauss points or lattices were involved in one 8-node element. Therefore, the cylinder specimen had 5,500 elements, which stand for 148,500 lattices. Several typical examples (Wang and Chen, 1997) show that the modified Gauss point method not only reduces the calculating time greatly but also guarantees the accuracy of the computation.

5 Results and Discussion

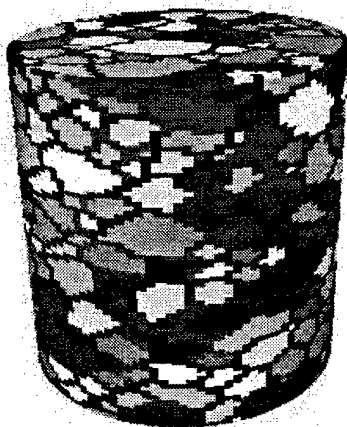
Results of the experimental measurements and numerical analyses are shown in Fig. 3 through 5. Very good agreement is found between displacement and stress (Fig. 3(a, b)). Fig. 4(a) shows the failure specimens by test, while Fig. 4(b) shows the damaged cylinders by numerical simulation at various confining pressures. Fig. 5 represents comparison of the angles of the failure planes by experimental and numerical analyses. It shows that a distinct failure surface or surfaces change orientation from vertical to angled as confinement increases. Based on this research, there are several points that need to be emphasized. First, confining pressure due to friction between platen and specimen has a predominating effect on the failure angle of a specimen under triaxial loading. It is essential to relieve the friction between the platens and the specimens. Second, to predict the failure mechanism accurately, randomly distributed cement paste and coarse aggregate is necessary in the simulation of 3-dimensional concrete specimen under triaxial loading.



$P = 0.0 \text{ Mpa}$



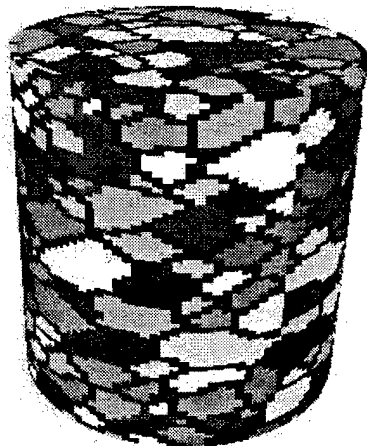
$P = 1.7 \text{ Mpa}$



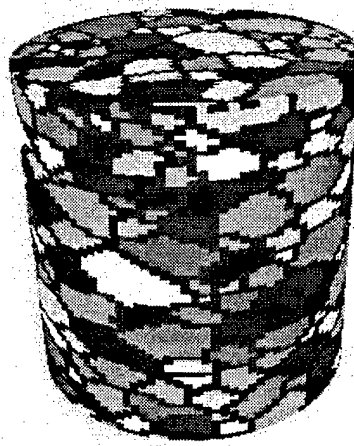
$P = 3.5 \text{ Mpa}$



$P = 7.0 \text{ Mpa}$



$P = 14.0 \text{ Mpa}$



$P = 28.0 \text{ Mpa}$

Fig.4(b) Damaged specimen by numerical simulation

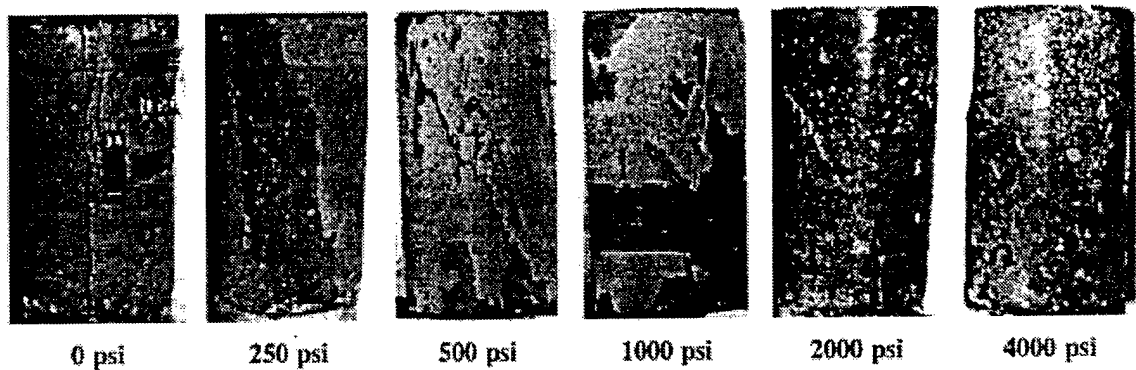


Fig.4(a). Damaged specimen by experiments

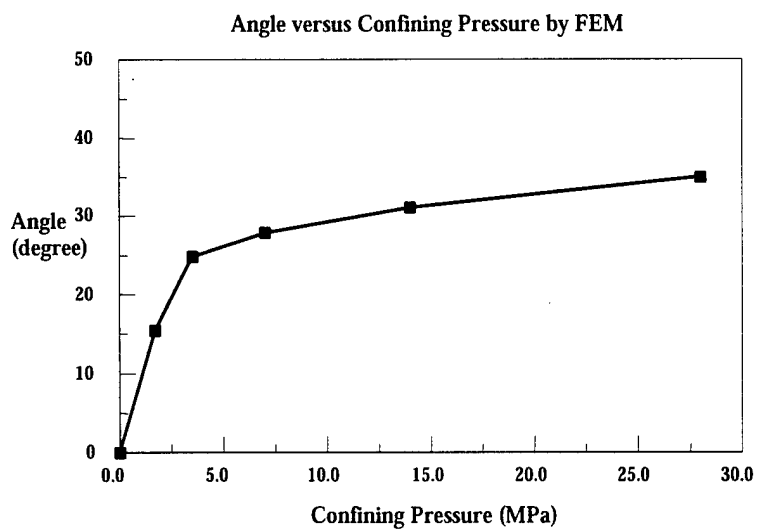
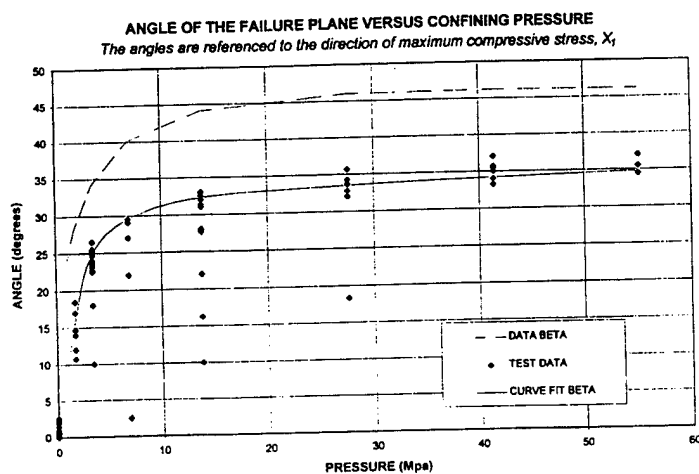


Fig.5. Angle versus confining pressure by test(a) and numerical simulation(b)

6 Conclusion

This study presented a procedure to predict the failure mechanisms of concrete under triaxial loading. Both experimental and numerical studies showed changes in the orientation of the failure plane as confining pressure increased for concrete cylinder specimens. For realistic triaxial loading in experiments, it is essential to relieve the friction between the platen and specimen. Based on comparison of experimental and numerical results, the strength ratio between cement paste (including interface) and coarse aggregate is randomly distributed between 0.1 to 0.4. It is strongly suggested that a realistic 3-dimensional meso-structure simulation be used in a numerical model. The presented modified Gauss point method is a key step to guarantee the efficiency and accuracy of the simulation.

7 References

- Desiderio, K. (1996) Grain size distributions and strength variability of high-purity alumina. **J. Am. Ceram. Soc.**, 79(2)305-12.
- Hockin, H. K. (1996). Influence of grain size on the grinding response of alumina. **J. Am. Ceram. Soc.**, 79(5)1307-13.
- Hassold, G. N. (1990). Computer simulation of final-stage sintering: I model, kinetic, and microstructure. **J. Am. Ceram. Soc.**, 73(10).
- Gerstle, K. H. (1980) Behavior of concrete under multiaxial stress states. **J. Eng. Mech. Division**, ASCE, 1383-1403
- Murrell, S.A. (1965) The effect of triaxial stress systems on the strength of rocks at atmospheric temperatures. **Geophys. J. R. Astron Soc.** 10, 231-281.
- Palaniswamy, R. (1972) Deformation and failure of hardened cement paste subjected to multiaxial stress. **Proc. of the RILEM**, 169-179.
- Wang, M. L. and Chen, Z. L. (1997). Modified Gauss point method and its application in THMs. **Proc. of Computer Aided Design of High-Temperature Materials**, Sante Fe, New Mexico, USA.
- Wang, M. L. and Rutland, C.A.(1995). Strain measurements using real time X-ray images, **Journal of British Society for Strain Measurement**, 'Strain' 87-94
- Wawersik, W.R. (19970) Post-failure behavior of a granite and diabase. **Rock Mechanics**, 3, 61-85
- Zimmerman, R.M. (1977) Strength and deformation response of concrete under multiaxial loadings-cooperative project. **Final Report ENG 74-12097** for NSF.

Simulation of the Failure Mechanisms of Quasi-Brittle Materials

M. L. Wang and Z. L. Chen

Department of Civil and Materials Engineering
University of Illinois at Chicago
Chicago IL 60607
USA

One of the major technical interests for quasi-brittle materials is the failure mechanism under uniaxial or triaxial loading, or under some other standard tests such as beam bending specimen and compact specimen. Recent research has led to development of formal procedures for predicting damage behavior of quasi-brittle material using computational simulation in the tests mentioned above. These procedures have subsequently been programmed into a computer module and thus have helped the researcher have a general direction of what the corresponding experiment will be. The objective of this paper is to present and describe results obtained using meso- or micro-mechanical simulation of quasi-brittle materials such as concrete and ceramic. Typical results show that the presented method provides a less expensive alternate to understanding the failure mechanisms of quasi-brittle materials.

Keywords: failure mechanism; quasi-brittle; structure simulation; modified Gauss point

Introduction

While the age of quasi-brittle materials including concrete and ceramic is upon us, the ability to accurately predict their performance mechanically has not yet arrived. In view of the difficulty in obtaining the failure mechanisms of these materials, one must often rely on both experimental and computational simulation, the latter provides a much less expensive alternative to the former.¹

Concrete and ceramics, being typical quasi-brittle materials, are widely used in advanced scientific experiments and applications. Computational simulation of

some of their standard tests gives the researcher an easy and less expensive way to master their failure mechanisms. Prior to numerical analyses, it is essential to establish a realistic 3-dimensional meso- or micro-structure simulation. Generally, hundreds and thousands of lattices or elements need to be included in the simulated model. This is extremely important because mechanical behaviors are determined by extremes in the local stresses, which have a close relationship with the distribution of grains and grain boundaries as well as grain size². Thus, in order to simulate the ceramics realistically, both in a geometrical and mechanical sense, enough simulated elements or lattices are essential.

In this paper, the Monte Carlo method is used to simulate the 3-dimensional microstructure. Because numerical analyses of a meso- or microstructure consume a lot of computer processing time, a modified Gauss point method is applied to reduce the processing time while still guaranteeing accuracy.

Meso- or Micro-Structure Simulation

In meso- or micro-scopic studies of quasi-brittle material such as concrete, it is necessary to generate a realistic 3-dimensional multiphase system consisting of cement paste and coarse aggregate³. As an example, a concrete cylinder specimen (Figure1) measuring 5 cm in diameter and 10 cm in height is divided into 148,500 lattices. Generally, that amount of lattices is necessary to reach a properly aggregated size of the given concrete specimen. Afterward, a non-zero index, which corresponds to both the phase and orientation of the aggregate, is initialized to each lattice by a random function. In a 2-phase simulation (α and β), the sign of S_i indicates the phase present at that site, while the absolute value of S_i corresponds to the orientation of the grain in which the site is embedded. Sites with one or more different closest neighbors are interface sites, sites with only like nearest neighbors are interior sites. Total system energy is specified by assigning a positive energy to interface areas (or cement pastes) and zero energy to the interior sites (or coarse aggregates), which can be calculated via the Hamiltonian equation

$$H = \frac{1}{8} \sum_{i=1}^N \sum_{j=1}^Z \left\{ (J_{\alpha\alpha} + J_{\beta\beta} + 2J_{\alpha\beta}) [1 - \delta(S_i, S_j)] + (J_{\alpha\alpha} + J_{\beta\beta} - 2J_{\alpha\beta}) \right. \\ \left. \text{Sign}(S_i) \text{Sign}(S_j) + (J_{\alpha\alpha} - J_{\beta\beta}) [\text{Sign}(S_i) + \text{Sign}(S_j)] \right\} \quad (1)$$

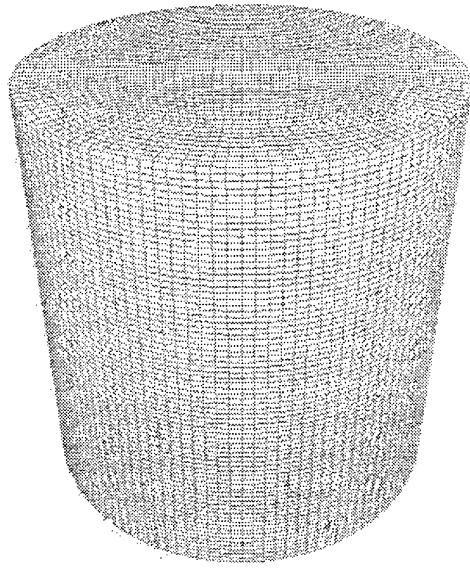


Figure 1 Specimen Lattice Plot Distribution



Figure 2 Specimen Aggregate Distribution

In equation (1), N is the total sites of the system. Z is the number of neighbors of the i^{th} site. δ is the Kronecker delta function. 'Sign' is the sign function defined as $\text{Sign}(S_i)$. It equals 1 if S_i is positive, and $\text{Sign}(S_i)$ equals -1 if S_i is negative. $J_{\alpha\alpha}$, $J_{\beta\beta}$ and $J_{\alpha\beta}$ are α - α , β - β , and α - β interfacial energies, respectively.

In iteration, the kinetic energy of the aggregate is adjusted by the Monte Carlo technique. First, a lattice site and a site index are chosen at random. The index of the chosen site is then changed to the new index if the corresponding total system energy, H , does not increase. After each attempted index change, the Monte Carlo step increases, and a simulated mesostructure is yielded. Figure 2 is a 3-dimensional simulated mesostructure plot of the cylinder specimen that involves 148,500 lattices. Different types of aggregates are composed of certain numbers of lattices, and between the aggregates are the interfaces or cement pastes.

The same procedures work for ceramic samples that include grains and their interfaces.

Model Description

Simulations of the static tests were performed using the finite element analysis code, which was developed for static analysis of nonlinear structural systems. The Drucker-Prager criterion and the low tensile strength criterion are applied.

An 8-node isoparameter 3-dimensional element is used in this code. Generally, the simulated model includes hundreds and thousands of lattices, each of them possessing different mechanical properties, such as ultimate strength and modulus of elasticity, which need to be incorporated in numerical analyses. However, it is very difficult or almost impossible to treat that many elements in finite element analysis due to the low efficiency and floating point errors of the calculation. The situation becomes even more difficult with nonlinear analysis.

Modified Gauss point method has been successfully used to reduce the computer processing time while still guaranteeing accuracy⁵. The basic idea of the modified Gauss point method used here is that each Gauss point in the numerical integration corresponds to one lattice and, therefore, one element involves a specific number of lattices, say 8 or 27 in a 3-dimensional problem. The Gauss point coordinates and the corresponding weight coefficients need to be modified because of the evenly distributed lattices. Table 1 lists the values of Gauss point coordinates, ξ_i , and the weighted coefficient, H_i , for the different number of Gauss points, n , evenly distributed between -1 and $+1$ in the case of 1-dimensional problem.

Table 1 Values of ξ_i Corresponding to Various n

n	H_i	ξ_i	Precise for m^{th} Order Polynomial
3	2/3	± 0.707107 0.0	$m=3$
4	2/4	± 0.794654 ± 0.187593	$m=4$ or 5
5	2/5	± 0.832497 0.0 ± 0.374541	$m=5$
6	2/6	± 0.866246 ± 0.422522 ± 0.374541	$m=5$ or 6

In this paper, 27 modified Gauss points or lattices are involved in one 8-node element. As an example, the cylinder specimen shown in Figure 1 has 5,500 elements which stand for 148,500 lattices. Numerical examples show that the

modified Gauss point method not only reduces the calculating time greatly but also guarantees the accuracy of the computation.

Numerical Examples and Discussions

1 Four Points Beam Bending

The chosen numerical example is the so-called four points beam bending problem (Figure 3). The beam has a cross section of 3 cm (height) \times 1 cm (width), and a span of 18 cm. The Young's modulus is 200 GPa, the Poisson ratio is 0.2, and the cohesive strength is 17 Mpa. The material of the beam is treated as a realistic elasto-plastic. Two models are taken into consideration:

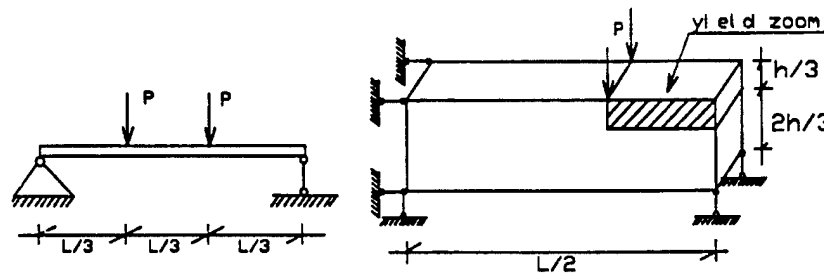


Figure 3 4-Points Beam Bending Specimen

(1) Common Gauss Point Method

$3 \times 3 \times 3$ Gauss points are used in one element to carry the numerical integration. A total of 216 elements are included in this model.

(2) Modified Gauss Point Method

$3 \times 3 \times 3$ lattices are included in each element. A total of 216×27 , or 5832 lattices are included in the second model.

The above two models produce the same numerical results. The yield zoom is shown in Figure 3 that occurs at $P = 2126$ N. Moreover, the two models consume almost the same amount of run time although the second one can simulate more

lattices than the first. Table 2 shows the comparison between the theoretical and numerical results.

Table 2: Comparison of Horizontal Stresses at $h/4$ in the Yield Zoom

	Theoretical	Numerical
Horizontal stress	29.45 MPa	29.31 MPa

This example suggests that although approximately the same amount of run time is consumed because they include the same number of integral Gauss points, the one using the modified Gauss point method could consider much more lattices and produce satisfactory result at the same time.

2 Cylinder Specimen under Triaxial Loading

This example describes the failure mechanisms of a concrete specimen under triaxial loading. The failure is characterized by a distinct failure surface or surfaces that change orientation from nearly vertical to angled as confining pressure increase.⁶ The simulated model that has 148,500 lattices is shown in Figure 2. After applying the modified Gauss point method, the specimen involves 5,500 elements.

Uniaxial displacement with a 5 μm in step is applied on the top of the specimen while a certain amount of confining pressure is exerted on the surrounding surface of the cylinder. Based on the results of the experiment,⁶ the friction between the platens and the specimen is relieved since this friction severely affects the development of the failure mechanisms as confining pressure increases.

Results of numerical analyses are shown in Figure 4 through 6. Very good agreement is found between displacement and stress (Figure 4(a, b)). Figure 5(a) shows the failure specimens by test, while Figure 5(b) shows the damaged cylinders by numerical simulation at various confining pressures. Figure 6 represents comparison of the angles of the failure planes by experimental and numerical analyses. It shows that a distinct failure surface or surfaces change orientation from vertical to angled as confinement increases. Based on this research, there are several points that need to be emphasized. First, confining pressure due to friction between platen and specimen has a predominating effect on the failure angle of a specimen under triaxial loading. It is essential to relieve

the friction between the platens and the specimens. Second, to predict the failure mechanism accurately, randomly distributed cement paste and coarse aggregate is necessary in the simulation of 3-dimensional concrete specimen under triaxial loading. Finally, to achieve the best results, simple and reliable nonlinear criteria should be chosen. For simplicity, criteria with easily determined parameters are recommended.

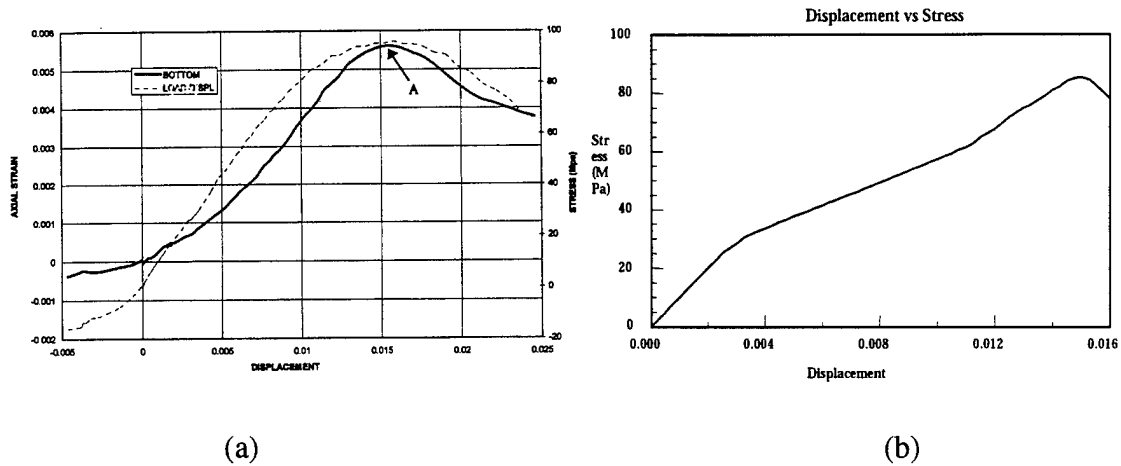


Figure 4 Typical Displacement-Stress Relationship: (a) Experimental Data and (b) Numerical Simulation (Units of Displacement is in cm)

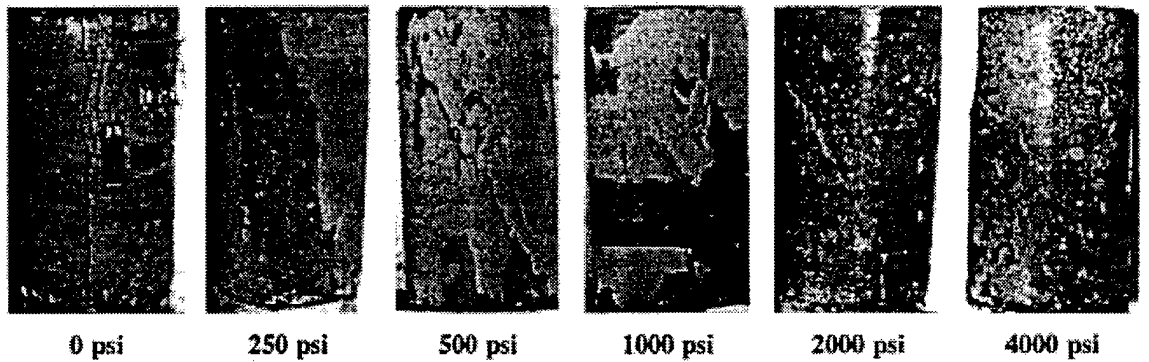
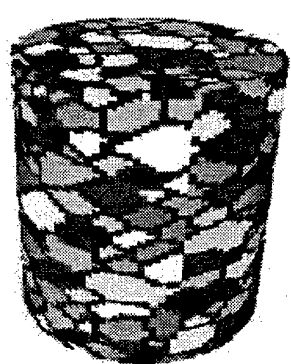


Figure 5(a). Damaged Specimen by Experiments



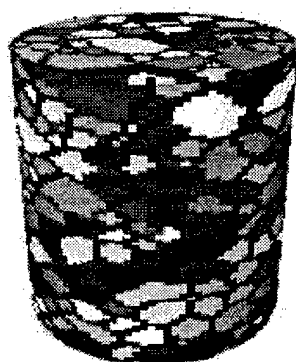
$P = 0.0 \text{ Mpa}$



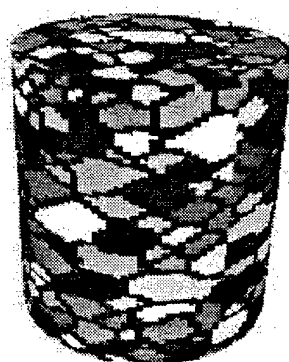
$P = 1.7 \text{ Mpa}$



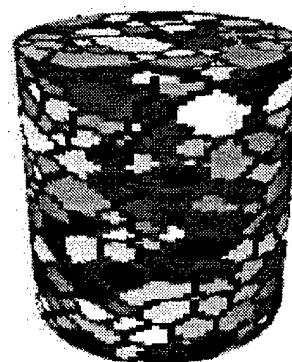
$P = 3.5 \text{ Mpa}$



$P = 7.0 \text{ Mpa}$



$P = 14.0 \text{ Mpa}$



$P = 28.0 \text{ Mpa}$

Figure 5(b) Damaged Specimen by Numerical Simulation

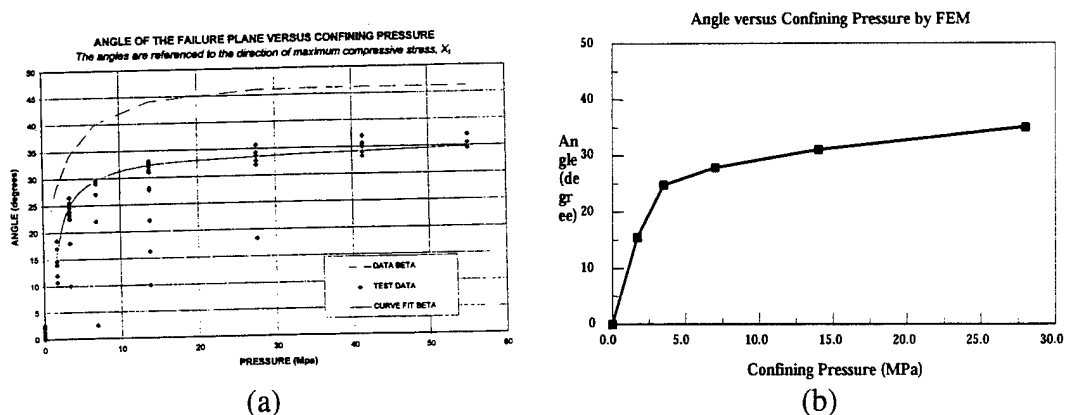


Figure 6 Angle versus confining pressure by test(a) and numerical simulation(b)

3 Compact Tensile Specimen

A compact tensile specimen was analyzed in this example. The configuration of the specimen was 25mm(width) \times 30mm(height) \times 1.5mm(depth). The specimen was loaded by a load-point displacement that is separated into 12 steps with 2.5 μ m each. A modified Gauss point method is applied in both of the following cases.

(1) The Effect of Grain Size

Two finite element models are put into consideration with total lattice numbers of 6701 and 15,182, respectively. Figures 7 and 8 show the grain size distributions with 800 and 1100 μ m, respectively. Figure 9 is the corresponding P_{eq} vs displacement plot that reveals that the smaller the grain size, the smaller the compact tensile P_{eq} . This conclusion is the same as mentioned in reference 7.

(2) The Effect of Boundary Conditions

Fixed and free boundary conditions are applied to the above specimen(Figure 10). This model has 6701 lattices and corresponding grain size is 1100 μ m as shown in Figure 7. Figure 11 is the plot of equivalent load P_{eq} vs applied known displacement, where P_{eq} is calculated by the equivalent condition. Figures 12 shows the comparison of the final damaged specimen with two different boundary conditions. According to the profiles of each step in simulation, the cracking starts from the crack tip and develops as the applying tensile force increases. Several single cracks occur during the simulation. Some of them develop while others stop cracking or even go back to closure. The final failure does not take place until one

or two main cracks reach the critical cracking length. Fig.13~15 are the experimental profiles of the cracking development that match the numerical simulation very well.

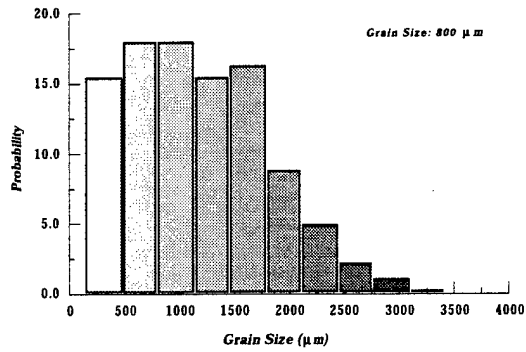


Figure 7 Grain Size Distribution

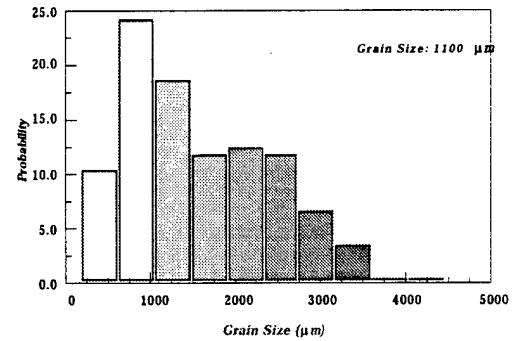


Figure 8 Grain Size Distribution

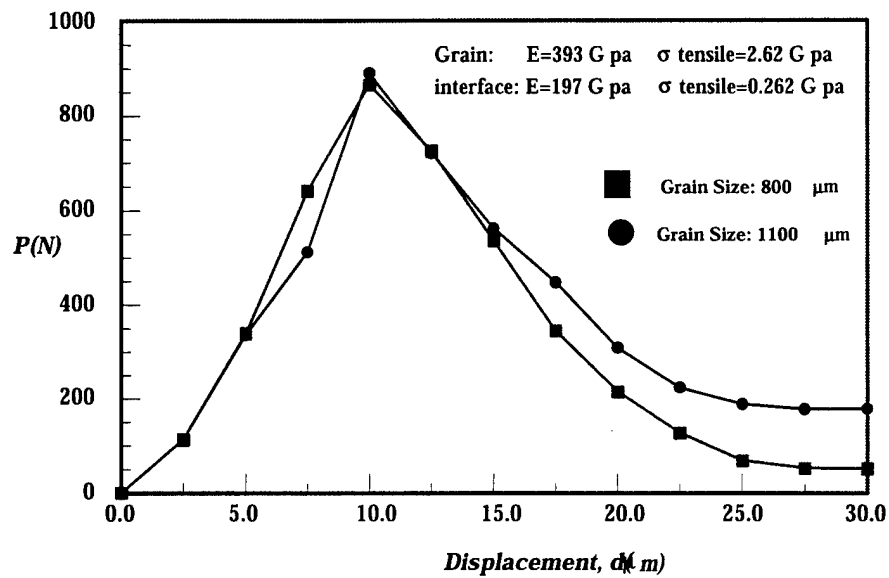
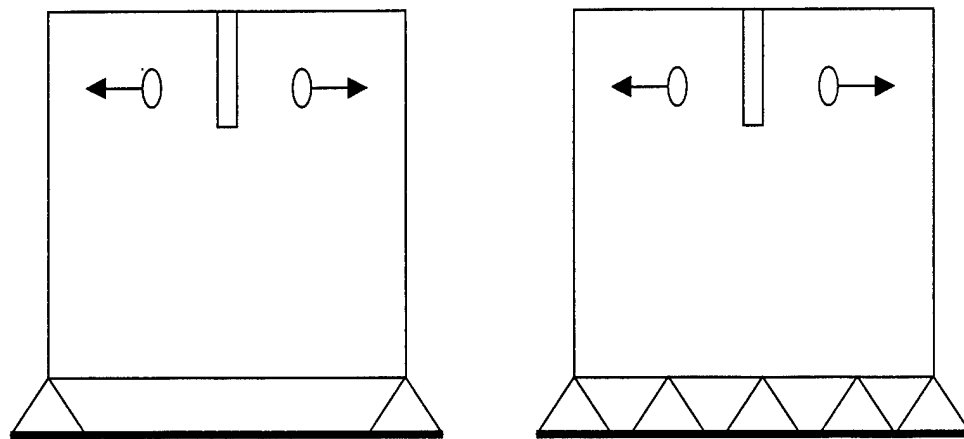


Figure 9 Effort s of Grain Size



Free Boundary Condition

Fixed Boundary Condition

Figure 10 Configuration of Specimen

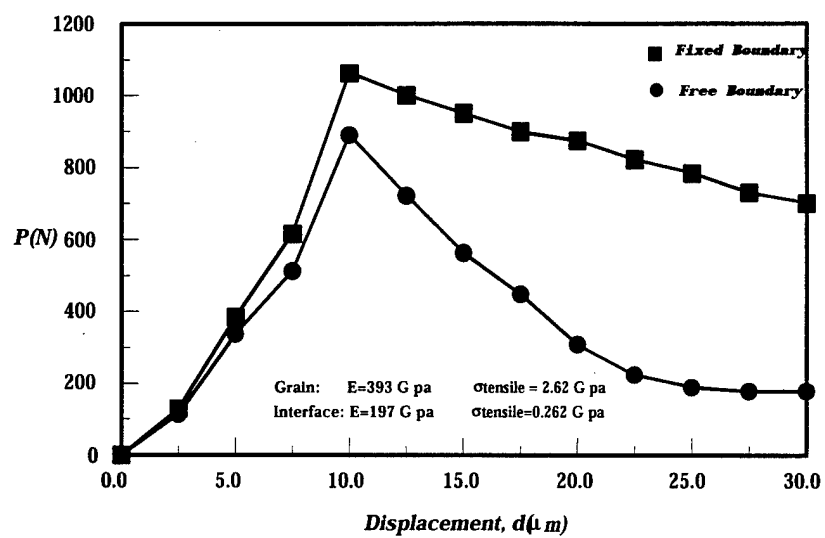
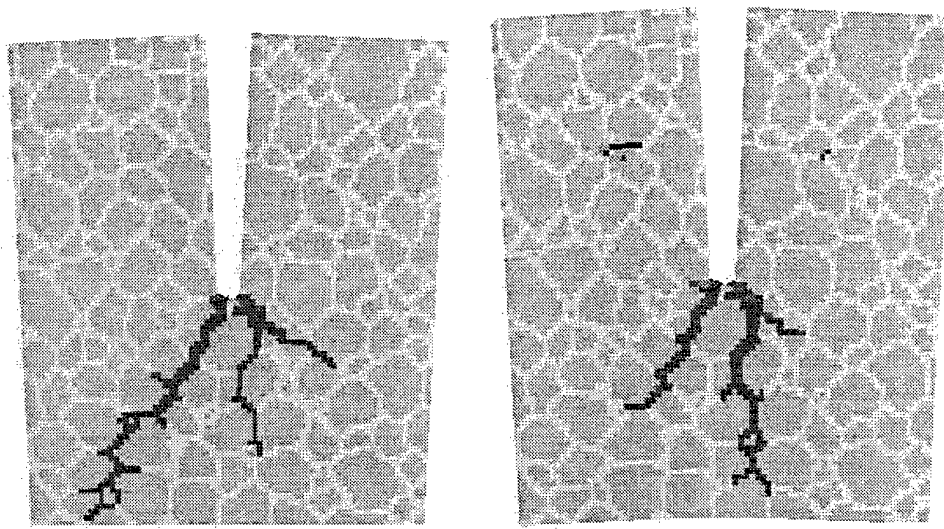


Figure 11 Effect of Boundary condition (Grain Size: 1100 μm)



(a)

(b)

Figure 12 Damaged Specimen (a) Fixed Boundary (b) Free Boundary Condition



Fig. 13 Microscope Profile of Cracking Specimen (Step 1)



Fig. 14 Microscope Profile of Cracking Specimen (Step 2)

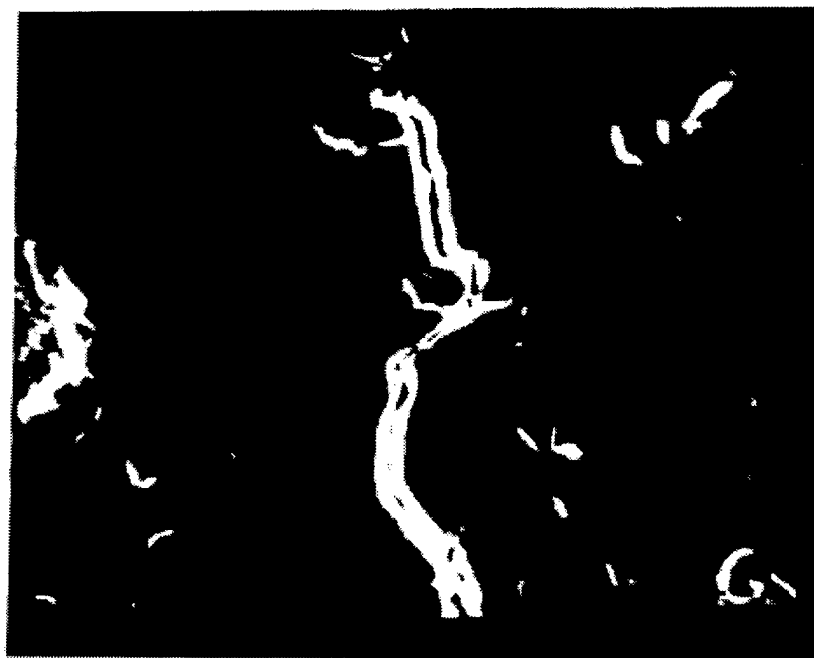


Fig. 15 Microscope Profile of Cracking Specimen (Step 3)

Conclusion

This study presented a procedure to predict the failure mechanisms of quasi-brittle materials under triaxial loading and some other standard tests. Prior to numerical analyses, it is essential to have a realistic 3-dimensional meso- or micro-structure simulation. The presented modified Gauss point method is another key step to guarantee the efficiency and accuracy of the simulation. The mechanical properties and failure mechanisms predicted by the above method are in good agreement with the previous experimental results. Thus, the method provides a less expensive alternative in understanding the failure mechanisms of quasi-brittle materials.

References

1. Subondh K. Mital, Computational simulation of intermingled-fiber hybrid composite behavior." *NASA TM*, 1992,105666.
2. Andreas K., Effects of grain size and humidity on fretting wear in fine-grained alumina, $\text{Al}_2\text{O}_3/\text{TiC}$, and Zirconia. *J. Am. Ceram. Soc.*,1996, 79(5), 1139-46.
3. Desiderio K., Grain size distributions and strength variability of high-purity alumina. *J. Am.Ceram. Soc.*, 1996, 79(2), 305-12.
4. Hockin, H. K., Influence of grain size on the Grinding response of alumina. *J. Am. Ceram. Soc.*, 1996, 79(5), 1307-13.
5. Wang, M. L. and Chen, Z. L., Modified Gauss point method and its application in THMs. *Proc. of Computer Aided Design of High-Temperature Materials*, 1997, Sante Fe, New Mexico, USA.
6. Rutland, C.A.and Wang M.L. The effects of confinement of the failure orientation in cemeticious materials. *Journal of Cement and Concrete Composites*, 1998, to be published
7. Robert F. Cook, Sigmodial Inedentation-strength Characteristics of Ploycrystalline Alumina. *J. Am.Ceram. Soc.* 1994, 77[2]303-14